

# Disentangling methane and carbon dioxide sources and transport across the Russian Arctic from aircraft measurements

Clément Narbaud<sup>1</sup>, Jean-Daniel Paris<sup>1,2</sup>, Sophie Wittig<sup>1</sup>, Antoine Berchet<sup>1</sup>, Marielle Saunois<sup>1</sup>, Philippe Nédélec<sup>3</sup>, Boris D. Belan<sup>4</sup>, Mikhail Y. Arshinov<sup>4</sup>, Sergei B. Belan<sup>4</sup>, Denis Davydov<sup>4</sup>, Alexander Fofonov<sup>4</sup>, Artem Kozlov<sup>4</sup>

<sup>1</sup> Laboratoire des Sciences du Climat et de l'Environnement, IPSL, Orme des Merisiers, CEA-CNRS-UVSQ, 91190 Gif-sur-Yvette, France

<sup>2</sup> Climate and Atmosphere Research Centre (CARE-C), The Cyprus Institute, Nicosia, 2121, Cyprus

<sup>3</sup> LAERO, Université de Toulouse, UT3, CNRS, IRD, Toulouse, France

<sup>4</sup> Independent researcher

*Correspondence to:* Jean-Daniel Paris (jean-daniel.paris@lsce.ipsl.fr)

**Abstract.** A more accurate characterization of the sources and sinks of methane (CH<sub>4</sub>) and carbon dioxide (CO<sub>2</sub>) in the vulnerable Arctic environment is required to better predict climate change. A large-scale aircraft campaign took place in September 2020 focusing on the Siberian Arctic coast. CH<sub>4</sub> and CO<sub>2</sub> were measured in situ during the campaign and form the core of this study. Measured ozone (O<sub>3</sub>) and carbon monoxide (CO) are used here as tracers. Median CH<sub>4</sub> mixing ratios are fairly higher than the monthly mean hemispheric reference (Mauna Loa, Hawaii, US) with 1890-1969 ppb vs 1887 ppb respectively, while CO<sub>2</sub> mixing ratios from all flights are lower (408.09-411.50 ppm vs 411.52 ppm). We also report on three case studies. Our analysis suggests that during the campaign the European part of Russia's Arctic and Western Siberia were subject to long-range transport of polluted air masses, while the East was mainly under the influence of local emissions of greenhouse gases. The relative contributions of the main anthropogenic and natural sources of CH<sub>4</sub> are simulated using the Lagrangian model FLEXPART in order to identify dominant sources in the boundary layer and in the free troposphere. In western terrestrial flights, air masses composition is influenced by emissions from wetlands and anthropogenic activities (waste management, fossil fuel industry and to a lesser extent the agricultural sector), while in the East, emissions are dominated by freshwaters, wetlands, and the oceans, with a likely contribution from anthropogenic sources related to fossil fuels. Our results highlight the importance of the contributions from freshwater and ocean emissions. Considering the large uncertainties associated to them, our study suggests that the emissions from these aquatic sources should receive more attention in Siberia.

## 1 Introduction

The increasing greenhouse gas burden in the atmosphere led to a global surface temperature rise. In the last decade (2011-2020), global surface temperature was 1.09 °C higher than the last decades of the 19th century (1850-1900) (Masson-Delmotte et al., 2021). The global mean mixing ratio of carbon dioxide (CO<sub>2</sub>) reached 413.2±0.20 ppm in 2020 (WMO, 2021). Anthropogenic CO<sub>2</sub> sources are dominated by fossil fuel combustion and cement production (9.6±0.5 GtC yr<sup>-1</sup>) and land-use

35 change ( $1.6 \pm 0.7 \text{ GtC yr}^{-1}$ ). While these emissions are steadily increasing, the main sinks of  $\text{CO}_2$ , terrestrial vegetation ( $3.4 \pm 0.9 \text{ GtC yr}^{-1}$ ) and oceans ( $2.5 \pm 0.6 \text{ GtC yr}^{-1}$ ) have taken up a rather stable proportion (about 56% per year) of emissions from human activities albeit with regional differences (Friedlingstein et al., 2020; Masson-Delmotte et al., 2021).

Methane ( $\text{CH}_4$ ), the second most abundant anthropogenic greenhouse gas, reached  $1889 \pm 2 \text{ ppb}$  in the atmosphere in 2020 (WMO, 2021), but has a global warming potential about 32 times higher than  $\text{CO}_2$  on a 100-year horizon (Etminan et al., 40 2016). Since 2007, the  $\text{CH}_4$  mixing ratio has been constantly increasing, up to  $8\text{-}9 \text{ ppb yr}^{-1}$  corresponding to an increase of the atmospheric burden of about  $25 \text{ Tg CH}_4 \text{ yr}^{-1}$  (Platt et al., 2018). A total of  $576 \text{ Tg CH}_4 \text{ yr}^{-1}$  has been injected into the atmosphere during the 2008-2017 decade combining anthropogenic and natural sources (Saunois et al., 2020). Anthropogenic emissions represent 60% of global total methane emissions with agriculture and waste management ( $191 \text{ to } 223 \text{ Tg CH}_4 \text{ yr}^{-1}$ ) and fossil fuel exploitation ( $113 \text{ to } 154 \text{ Tg CH}_4 \text{ yr}^{-1}$ ) (Saunois et al., 2020). On a global scale, wetlands are the largest natural methane 45 emission source ( $153 \text{ to } 227 \text{ Tg CH}_4 \text{ yr}^{-1}$ ) (Kirschke et al., 2013; Lan et al., 2021). Emissions from freshwaters have estimates ranging widely between  $60 \text{ and } 180 \text{ Tg CH}_4 \text{ yr}^{-1}$  (Saunois et al., 2016) and are mainly driven by diffusion, ebullition and release from bubble storage (Matthews et al., 2020). Fluxes from aquatic sources may be underestimated (Rosentreter et al., 2021). Ocean emissions by diffusion and ebullition are estimated to range between  $2 \text{ and } 40 \text{ Tg CH}_4 \text{ yr}^{-1}$ . However, these estimated  $\text{CH}_4$  emissions could potentially be higher due to large gas hydrate reservoirs on the seabed of Arctic Ocean (Platt et al., 2018). 50 Widely debated emissions attributed to marine sources including methane hydrates dissociation have already been observed in the region (Shakhova et al., 2010; Berchet et al., 2016; Platt et al., 2018; Berchet et al., 2020; Thornton et al., 2020; Steinbach et al., 2021).

Siberia and the Russian Arctic are significant contributors to the  $\text{CH}_4$  budget. Half of Siberian emissions originate from fossil fuel exploitation (about  $17 \text{ Tg CH}_4 \text{ yr}^{-1}$ ), one third from natural wetlands (about  $13 \text{ Tg CH}_4 \text{ yr}^{-1}$ ) and a minor contribution from 55 agriculture and waste (about  $5 \text{ Tg CH}_4 \text{ yr}^{-1}$ ) for a total average of  $38 \text{ Tg CH}_4 \text{ yr}^{-1}$  (Saunois et al., 2016). The multiplicity of the sources and the seasonality of emissions (Berchet et al., 2015; Belikov et al., 2019) influence  $\text{CH}_4$  variability over Siberia. Many uncertainties in the  $\text{CH}_4$  emissions in Siberia therefore remain (Berchet et al., 2016; Elder et al., 2020; Matthews et al., 2020; Wik et al., 2016; Thornton et al., 2016). Uncertainties are driven by the multitude of adjacent sources present in the region: natural wetlands, freshwaters (lakes, ponds and streams), oceans and anthropogenic activities (leaks from increasing 60 oil and gas extraction and transport, as well as regional agriculture and waste management) and biomass burning. In addition to the currently dominant sources, the thawing of continental and submarine permafrost could release massive amount of carbon in the atmosphere since Siberia is considered to be one of the world's largest terrestrial carbon reservoirs (Belikov et al. 2019). Soils in the permafrost region retain twice as much carbon as the atmosphere does (Turetsky et al., 2019).

To reduce uncertainties at the scale of Siberia, atmospheric measurements have been performed at tower observatories (Belikov 65 et al., 2019; Sasakawa et al., 2010; Sasakawa et al., 2017; Fujita et al., 2020), during oceanographic campaigns (Thornton et al., 2016; Berchet et al., 2020; Steinbach et al., 2021) or even by train (Skorokhod et al., 2016). The YAK-AEROSIB project organizes intensive campaigns since 2006 across all of Siberia (Paris et al., 2008; Paris et al., 2010a). These annual campaigns

provide measurements of atmospheric concentrations of CO<sub>2</sub>, CH<sub>4</sub>, O<sub>3</sub>, carbon monoxide (CO) and aerosols with an objective to better understand regional sources, dynamical processes and long-range transport in Siberia (Paris et al., 2008; Berchet et al., 2013). In situ measurements have the potential to document carbon sources and sinks in Siberia, and therefore to ultimately establish a more accurate estimation of future greenhouse gas trajectories. The previous campaigns have highlighted several key mechanisms in this poorly-studied region by representing vertical profiles of several greenhouse gases to determine the origin and impact of polluted air masses (Paris et al., 2008), identifying the source of upper tropospheric O<sub>3</sub> depletion (Berchet et al., 2013) or also bringing new insights on specific events like the extensive wildfires that occur in Siberia during summer (Paris et al., 2009; Antokhin et al., 2018). In the present work, we analyze data from the last YAK-AEROSIB campaign that took place during September 2020 with a specific focus on Northern Russia and the coastal Arctic Ocean. This campaign included 13 flights across Russia with dedicated flights over the northern seas of Barents, Kara and Laptev, and the very East of the region with Bering Strait, the East Siberian Sea and the Chukchi Sea.

The present study focuses on the distribution of CH<sub>4</sub> and CO<sub>2</sub>. This paper aims more specifically to identify and quantify the respective contributions from regional sources of CH<sub>4</sub> during the first half of September 2020 in the Russian Arctic. We document the measurement and data collected during the campaign. Ozone and carbon monoxide are used as tracers for the interpretation of CO<sub>2</sub> and CH<sub>4</sub> mixing ratio variability. Tropospheric ozone is a harmful pollutant produced from precursors including CO and CH<sub>4</sub> (Saunio et al., 2016), while CO is a pollutant and a minor greenhouse gas produced by combustion processes.

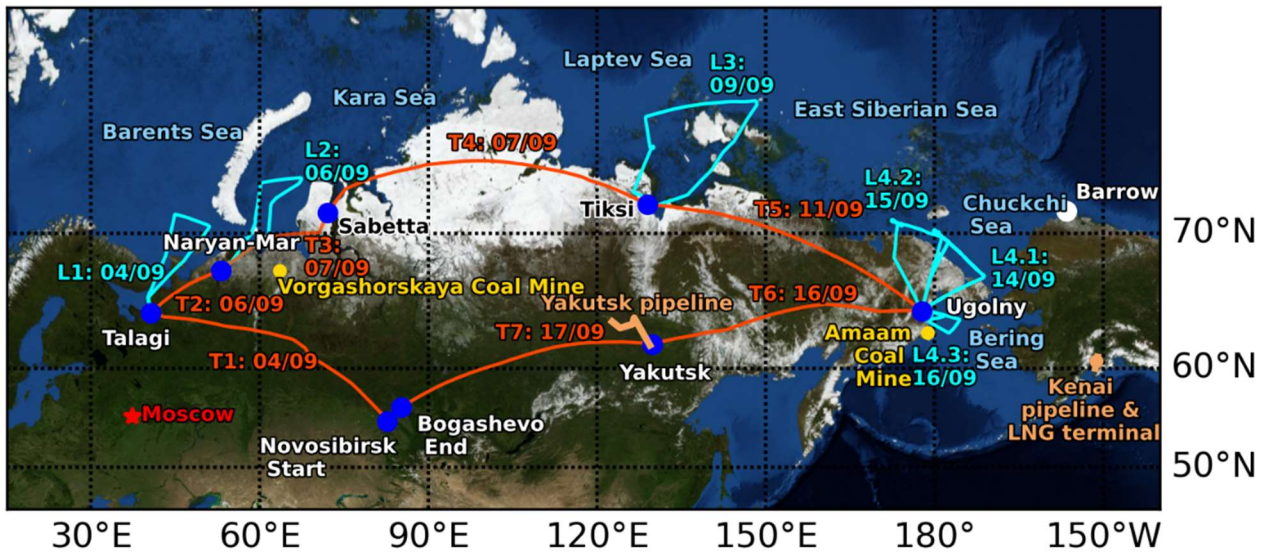
In Sect. 2, we first describe the study area and the in-situ instrumentation for continuous measurements of CO<sub>2</sub>, CH<sub>4</sub>, O<sub>3</sub>, and CO. We also explain our approach and the inputs to determine the contributions of each CH<sub>4</sub> source to the measurements made during the campaign, which is mainly achieved by combining the Lagrangian FLEXible TRAjectory model (FLEXPART) of transport and diffusion, with methane flux inventories. In Sect. 3 we present the 47 vertical profiles taken during the campaign with an emphasis on CO<sub>2</sub> and CH<sub>4</sub> mixing ratios. We then focus on four individual vertical profiles to characterize atmospheric transport of three different regions. We also discuss how the data coincide with simulations of CH<sub>4</sub> enhancements linked to anthropogenic and natural sources to give insights on the main CH<sub>4</sub> contributions at the time of the flight. We conclude by discussing the respective importance of anthropogenic activities and aquatic sources on CH<sub>4</sub> variability over Western Russia and Northeastern Siberia.

## 95 **2 Methods**

### **2.1 Description and synoptic situation of the campaign**

The flight route of the September 2020 campaign is shown in Fig. 1 and the campaign is described in Table 1. An overview of the campaign can be found in Belan et al. (2022). The aircraft used for the campaign was the “Optik” Tupolev-134A-3M (SKh)

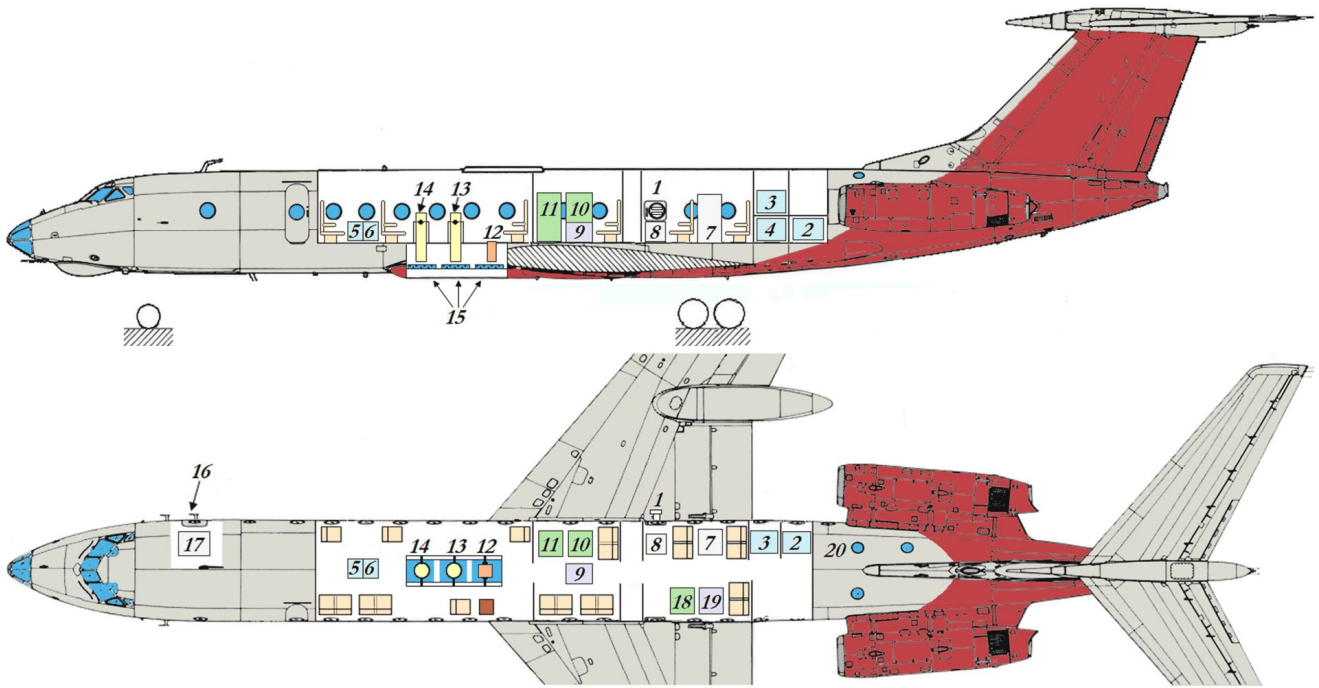
operated by the V.E. Zuev Institute of Atmospheric Optics (Tomsk, Russia) (Antokhin et al., 2018; Belan et al., 2022). The maximum range of the plane is 3000 km with an average observed airspeed of  $172 \text{ m s}^{-1}$  and a vertical speed of  $6.5 \text{ m s}^{-1}$  for both ascents and descents. The plane configuration is illustrated in Fig. 2 and more details can be found in Belan et al. (2022). The campaign took place between September 4<sup>th</sup> and 17<sup>th</sup>, 2020. The period of the campaign was chosen to be during summer to have measurements when the ocean is open. While September is not expected to be a period of maximum emissions, it presents minimum sea ice (Fig. A1) and maximum thaw. Thirteen different flights covered Russia from  $55^\circ \text{ N}$  to  $76^\circ \text{ N}$  between  $40^\circ \text{ E}$  and  $172^\circ \text{ W}$  for a cumulative ground distance of 25000 km with altitudes up to 11 km. The flights are grouped in two different categories: 1) loops above lands and oceans to explore specific environments with flight legs at typical altitudes of 200, 500 and 5000 m (these flights are referred to with a prefix “L”), and 2) transit flights between airports (prefix “T”). The campaign started in Novosibirsk and ended in Bogashevo (Tomsk airport). The first flights (T1, L1, T2, L2 and T3) crossed the cities of Arkhangelsk and Naryan-Mar and encompassed different biomes such as taiga (boreal forest), extensive wetlands and steppe regions (Belikov et al., 2019). Then the plane travelled along the Northern shores of the Russian Federation (T4, L3 and T5), above section of the Arctic Ocean in the seas of Kara, Laptev and the East Siberian Sea, crossing the small towns of Sabetta and Tiksi. The Arctic Ocean is at its lowest annual sea-ice extent in September and September 2020 was the second record low in Arctic sea-ice extent after 2012 (Fetterer et al., 2017). The seas that were covered by the campaign were essentially free of ice during the campaign (Fig. A1). The East Siberian Arctic Shelf (ESAS) contains up to 40% of Arctic marine permafrost (Ruppel, 2015). Several loops (L4.1, L4.2, and L4.3) were carried out in the Russian Far East characterized by Arctic deserts, tundra, and forest tundra for the northern regions while the south is dominated by forests (Petäjä et al., 2021). All these loops used the airport of Ugolny (Anadyr). The final transit flights (T6 and T7) crossed regions covered by forests of coniferous trees and by agricultural lands to the South (Bartalev et al., 2003), and landed at the airports of Yakutsk and Tomsk respectively. Large oil and gas (O&G) infrastructures (Yakutsk pipeline, Kenai terminal in Alaska) and coal mines (Ammam, Vorgashorskaya) from the Global Monitor Energy (2022) database are displayed on the map.



125 Figure 1: September 2020 campaign flight plan. The 13 flights are indicated either as “loop” (prefix L, cyan line) or “transit” (prefix T, orange line). Oil and gas (O&G) infrastructures and coal mines are shown in light orange and yellow respectively (data from “Global Coal Mine Tracker” and “Global Fossil Infrastructure Tracker”, Global Energy Monitor 2022, under CC BY-NC-SA 4.0 License). Map background: “Blue Marble Next Generation”, September 2004 (Stöckli et al., n.d.).

Table 1: Campaign description

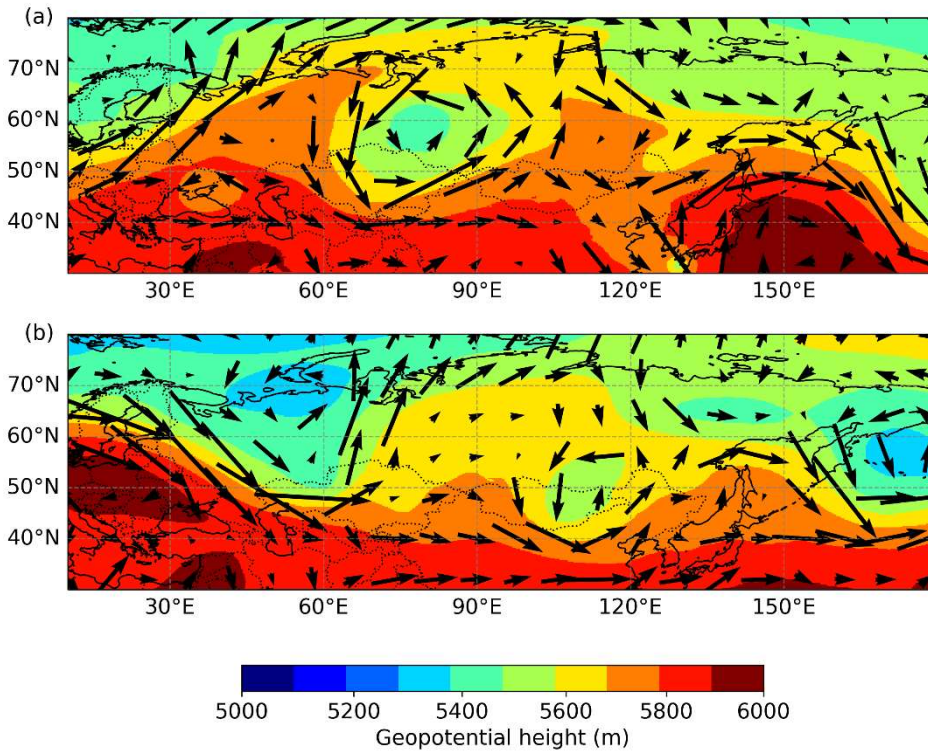
| Flight | Date UTC       | Time UTC    | Local Time  | Airports                 | Latitude | Longitude  |
|--------|----------------|-------------|-------------|--------------------------|----------|------------|
| T1     | 04 Sept. 20    | 06:55-11:01 | 13:55-15:01 | Novosibirsk North-Talagi | 55-65° N | 83-41° E   |
| L1     | 04 Sept. 20    | 12:58-17:06 | 15:58-20:06 | Talagi                   | 65° N    | 41° E      |
| T2     | 06 Sept. 20    | 08:07-09:31 | 11:07-12:31 | Talagi-Naryan Mar        | 65-68° N | 41-53° E   |
| L2     | 06 Sept. 20    | 10:55-14:36 | 13:55-17:36 | Naryan Mar               | 68° N    | 53° E      |
| T3     | 07 Sept. 20    | 05:01-06:27 | 08:01-11:27 | Naryan Mar-Sabetta       | 68-71° N | 53-72° E   |
| T4     | 07 Sept. 20    | 08:14-10:48 | 11:14-19:48 | Sabetta-Tiksi            | 71-72° N | 72-129° E  |
| L3     | 09 Sept. 20    | 03:09-06:57 | 12:09-15:57 | Tiksi                    | 72° N    | 129° E     |
| T5     | 11 Sept. 20    | 01:48-05:00 | 10:48-17:00 | Tiksi-Ugolny             | 72-65° N | 129-178° E |
| L4.1   | 14-15 Sept. 20 | 23:28-02:57 | 11:28-14:57 | Ugolny                   | 65° N    | 178° E     |
| L4.2   | 15-16 Sept. 20 | 22:32-01:42 | 10:32-13:42 | Ugolny                   | 65° N    | 178° E     |
| L4.3   | 16 Sept. 20    | 03:38-05:51 | 15:38-17:51 | Ugolny                   | 65° N    | 178° E     |
| T6     | 16-17 Sept. 20 | 23:16-02:39 | 11:16-11:39 | Ugolny-Yakutsk           | 65-62° N | 178-130° E |
| T7     | 17 Sept. 20    | 03:57-07:49 | 14:57-14:49 | Yakutsk                  | 62° N    | 130° E     |



130 **Figure 2: Arrangement of the instrument suite on board the OPTIK TU-134 aircraft laboratory: 1 – ambient air inlets and RH&T**  
**probe; 2 – aircraft electrical power distribution unit (28 VDC); 3, 4, 5, 6 – inverters (28 VDC/220 VAC) and UPSs (Delta RT-2K);**  
**7 – aerosol instrument rack: Aethalometer (MDA-02) and photoelectric aerosol nephelometer (FAN-M); 8 – aerosol instrument**  
**rack: diffusional particle sizer (DPS), optical particle counter (Grimm 1.109), filter, and bioaerosol sampling suite; 9 – navigation**  
**system (CompaNav-5.2 IAO); 10 – gas analysis rack: CO<sub>2</sub>–CH<sub>4</sub>–H<sub>2</sub>O (Picarro G2301-m): 11 – gas analysis rack: O<sub>3</sub> (TEI model**  
135 **49C), CO (TEI model 48C); 12 – spectroradiometer (Spectral Evolution PSR-1100F); 13, 14 – aerosol lidars; 15 – camera hatches;**  
**16 – ambient air inlet; 17 – sampling unit for organic aerosol analysis; 18 – gas analysis rack: NO<sub>x</sub> (Thermo Scientific model 42i-**  
**TL); 19 – main data acquisition system (NI PXI-1042); 20 – GLONASS/GPS antennas. Figure and caption by Belan et al. (2022).**

Figure 3 shows the geopotential height at 500 hPa as provided in the dataset ERA5 from the European Centre for Medium-  
140 Range Weather Forecasts; (ECMWF; Hersbach, 2018) on the 6<sup>th</sup> and the 15<sup>th</sup> of September. At the beginning of the campaign  
(Fig. 3a), there were a low-pressure system over central Siberia (80° E, 60° N) and a high-pressure ridge coming from Western  
Europe and going in a north-easterly direction to the seas of Barents and Kara. The period was characterized by an “Omega”  
whirling around troughs over Eastern Europe and eastern Asia that can be seen distinctly at the end of the campaign (Fig. 3b).  
The combination of these two events lifted an air mass most likely affected by western European emissions into the free  
145 troposphere over Siberia during the campaign. This may have influenced greenhouse gases concentrations as measured during  
the campaign. Over Eastern Siberia (180° E, 55° N), there was a low-pressure system and winds blown from western Alaska  
to Bering Strait (Fig. 3b).





150 **Figure 3: (a) Geopotential height and wind (speed and direction) at 500 hPa from ECMWF reanalyses for 06 September at 13:00 UTC. (b) Same as (a) for 15 September at 01:00 UTC**

A series of 47 vertical profiles was collected, each lasting between 20 and 30 min. Loop flights were composed of three ascending and descending profiles. Transit flights had only vertical profiles during take-off and landing, and took place at high altitude (about 10 km) in between. The plane stayed at horizontal plateaus when top altitudes were reached between 9000 m and 11000 m, as well as close to the ground at about 200 m and some on descents at 5000 m and at 500 m. About 80% of the data was acquired above 2000 m which is generally above the planet boundary layer (BL) at these latitudes and time of the year. 60% of the measurements were taken North of the Arctic Circle ( $> 66^\circ \text{N}$ ).

## 2.2 Instrumentation of the campaign

160 For in situ analysis air is sampled from inlets. The length of the tubes between the inlets and instruments was 4.8 m. Mixing ratios of  $\text{CO}_2$  and  $\text{CH}_4$  were measured by a Picarro G2301-m GHG analyzer using Cavity Ring-Down Spectroscopy. It is a modification of the G2301 model specially conceived for aircraft measurements which is designed to minimize effects induced by aircraft vibration and roll, and suitable for rapidly changing altitude (up to  $1000 \text{ m min}^{-1}$ ). It has an acquisition rate of 1 Hz and a precision of  $<0.20 \text{ ppm}$  for  $\text{CO}_2$  and  $<1.5 \text{ ppb}$  for  $\text{CH}_4$ . Water vapor mole fraction is also quantified to include internal

water dilution correction and thereby express dry air mixing ratios of carbon dioxide and methane. Three calibration gases are transported in high-pressure cylinders with respective CO<sub>2</sub> mixing ratios of 370.91±0.005 ppm, 390.33±0.009 ppm and 430.30±0.006 and CH<sub>4</sub> mixing ratios of 1814.35±0.150 ppb, 1960.99±0.094 ppb, and 2205.01±0.106 ppb. Their values were determined before the campaign at Laboratoire des Sciences du Climat et de l'Environnement (LSCE) according to World Meteorological Organization (WMO) standards (Paris et al., 2008). The drift is then corrected according to the difference between the measurements and the calibrated value of the reference gas. The whole campaign has been sampled at an interval of 1 s without data gaps, except for the transit T1 (the first of the series) during which the instrument software “froze” for the first half of the flight and was restarted after. The calibrated measurements can be compared to values of stations considered as reference sites for species measured during September 2020:

- Mauna Loa, Hawaii (19.54° N, 155.58° W, 3397 m a.s.l) (Oltmans and Levy 1994; Dlugokencky et al., 2021a; Dlugokencky et al., 2021b) for CO<sub>2</sub>, CH<sub>4</sub> and O<sub>3</sub>.
- Mace Head marine sector, Ireland (53.20° N, 09.54° W, 25 m a.s.l) (Hazan et al., 2016) for CO<sub>2</sub>, CH<sub>4</sub> and CO. Marine sector means that a selection on data based on standard deviation, wind speed and wind direction has been made to only keep air masses from westerly sectors (Biraud et al., 2000).
- Barrow, Alaska (71.32° N, 156° W, 11 m a.s.l, see Fig. 1) for CO<sub>2</sub> and O<sub>3</sub>.

Ozone was measured by a commercial fast response ozone analyzer (Thermo Environmental Instruments Model 49C USA), with modifications for internal calibration and aircraft operation safety. It is based on UV absorption in two parallel cells and has a precision of 2 ppb for an integration time of 4 s. In practice, values have been acquired with periods that vary between 4 and 10 s. Air is pressurized prior to the detection by a Teflon KNF Neuberger pump model N735 also used for CO. Before the campaign, the instrument has been calibrated against a NIST related reference calibrator Model49PS and verification of the O<sub>3</sub> analyzer have been made before and after the campaign. The length of the Teflon tubes between the inlet and O<sub>3</sub> and CO analyzers was 2m.

Carbon monoxide is acquired by an instrument based on a commercial infrared absorption correlation gas analyzer (Thermo Electron Model 48C, USA). It has been improved with addition of a periodical in-flight accurate zero measurements, new IR detector, pressure increase and regulation in the absorption cell, increased flow rate to 4 l min<sup>-1</sup>, water vapor trap and ozone filter. The response time of the instrument is 30 s and it has a precision of 5 ppb, with a lower detection limit at 10 ppb (“YAK-Aerosib Measurements”, 2021). For this campaign, the CO data were not post-processed due to technical problems and were therefore of lower quality than in previous studies. We applied a median filter with a kernel size of 75 samples. When computing the statistics for each flight, CO standard deviations were ranging between 10 and 35 ppb for mean mixing ratios between 73 and 103 ppb. In the present study, CO measurements are discussed as tracer for analysis of the other gases. To be compared with simulations (see Sect. 3.4), the measured mixing ratios were 1-minute averages with the background removed. The background is defined for each flight as follows: 1) only CH<sub>4</sub> values in air that had a corresponding O<sub>3</sub> mixing ratio < 70



ppb were kept, to remove influence from air of fresh stratospheric origin. 2) Then the 5th percentile of the remaining data was taken as the background value. Background mixing ratio were calculated flight by flight.

### 2.3 Back trajectories with the Lagrangian model FLEXPART

200 We used the Lagrangian particle transport and dispersion model FLEXPART (Stohl et al., 1998; Stohl and Thomson 1999; Stohl et al., 2005; Pisso et al., 2019) for long-range transport analysis and for determining the origin of the polluted air masses measured during the campaign. We adopted the backward (“receptor-oriented”) approach of the model suitable when the number of sources is superior to the number of receptors and designed to quantify the remote contributions in a single plume (Seibert and Frank 2004). In our configuration FLEXPART computed the position of 2000 particles backwards in time, following the atmospheric conditions with a stochastic contribution representing the diffusion (including small scale turbulence not included in averaged meteorological fields) (Fleming, Monks, and Manning 2012). These implementations allowed a more realistic representation of transport in planet boundary layer. The lifespan of the virtual particles was set to 10 d as the transport precision decreases after 10 days due to accumulated transport errors and insufficient number of particles to represent it (Stohl et al., 1995). The meteorological inputs were ERA5 datasets from ECMWF with a spatial resolution of 1° and a temporal resolution of 3 h covering the north hemisphere, limiting the resolution of the output grid to 0.5° x 0.5°. A simulation was performed for each flight, beginning 10 days before the first acquisition and ending with the last acquisition. Receptor (i.e. aircraft) positions every 1 s during the campaign are aggregated in four dimensions boxes (0.1° x 0.1° x 100 m x 60 s). The potential emission sensitivity (PES) calculated by the model for each receptor position is defined as the residence time of the backward particles in a grid cell below a threshold altitude (here 500 m and 2000 m). We convolved this output with CH<sub>4</sub> flux inventories to get maps of potential sources contributions that are integrated over the Northern Hemisphere to finally get the simulated mixing ratios of each source every minute.

### 2.4 Methane flux inventories

For our simulations, five categories of CH<sub>4</sub> sources were considered:

- 220 - Emissions of CH<sub>4</sub> by anthropogenic activities were characterized with EDGAR v6.0 (Emission Database for Global Atmospheric Research from PBL Netherlands Environmental Assessment Agency) with a grid resolution of 0.1° x 0.1° (Crippa et al., 2019). EDGAR inventories are published as yearly or monthly files. We chose to use the month of September 2018 (the last available) to benefit from the seasonality of the emissions. We aggregated the 21 EDGAR sectors into three categories: agriculture, exploitation and use of fossil fuels and waste management (see grouping definition in Table B1).
- 225 - Biomass burning and wildfires emissions were represented using GFED4.1s (Global Fire Emissions Database) based on van der Werf et al. (2017) at a resolution of 0.25° x 0.25° for the monthly mean of September 2020.

- Wetland fluxes were based on the process-based model ORCHIDEE as described in Ringeval et al. (2012) at a horizontal resolution of  $0.5 \times 0.5^\circ$  for September 2017 only for the North Hemisphere provided to Global Carbon Project 2019 (Melton et al., 2013; Wania et al., 2013; Zhang et al., 2021).
- 230 - The representation of freshwater  $\text{CH}_4$  fluxes, based on the work of Thonat et al. (2017), combined two inventories: the lake biogeochemical model (Blake4me) (Tan et al., 2015) for sources above  $60^\circ \text{N}$  and Global Lakes and Wetlands Database (GLWD3) distribution for the rest of the Northern Hemisphere (Lehner and Döll, 2004), with a resolution of  $0.25^\circ \times 0.25^\circ$  based on data from 1971 to 2013.
- The ocean fluxes were based on the work of Weber et al. (2019), a synthesis of measurements made between 1980  
235 and 2016 with an output grid in resolution  $0.25^\circ \times 0.25^\circ$  from the Marine Methane and Nitrous Oxide (MEMENTO) database (Kock and Bange, 2015). The total marine fluxes are provided as diffusive fluxes from sediments to the surface and ebullition of bubbles released from bottom sediments that reached the atmosphere. We combined the two fluxes in one emission map.

When it was possible, we preferred using inventories averaged on September instead of inventories averaged on several months  
240 to put an emphasis on the seasonality of emissions. All inventories were re-gridded to  $0.5^\circ \times 0.5^\circ$  in order to be aligned with the grid of the FLEXPART footprints. Figure B1 illustrates the fluxes indexed by inventories from fossil fuel emissions, agriculture, wetlands, freshwaters, and oceans on Northern Hemisphere.

### 3 Results

#### 3.1 Distribution of $\text{CH}_4$ and $\text{CO}_2$ during the campaign

245 Hereafter we refer to “low altitude” and “high altitude” for data that are respectively acquired below and above an arbitrary altitude threshold of 2000 m. The majority (80 %) of the data have been measured at “high altitude”. “Low altitude” measurements are analyzed separately to highlight sensitivity to local or regional sources. Reported uncertainties are  $1\sigma$  uncertainties.

##### 3.1.1 $\text{CH}_4$ mixing ratios

250 The average  $\text{CH}_4$  mixing ratio of the campaign is  $1946 \pm 45$  ppb. This is higher than the monthly mean mixing ratio measured at Mauna Loa 1887 ppb used as Hemispheric reference. Figure 4a shows that the median value of each flight (except for T6) is above the Mauna Loa mean value. At low altitude, the average mixing ratio is higher with a value of  $2011 \pm 33$  ppb and so exceed mixing ratios observed at Mauna Loa, Mace Head marine sector (1956 ppb) and Barrow (1991 ppb). This suggests the possible influence of significant regional methane sources. Many flights present a high  $\text{CH}_4$  variability. Flights in the western  
255 Siberian Arctic have the highest 3<sup>rd</sup> quartile of the campaign (L1, L2 and T2) then followed by the flights in the eastern Arctic (L3, L4.2 and L4.3). Large mixing ratio are expected to be encountered in the boundary layer, linked to regional sources, these

will be discussed in the Sect. 3.2 by using vertical profiles. Flights T1 and T6 registered the lowest CH<sub>4</sub> mixing ratios of the campaign (respectively 1812 ppb and 1777 ppb with an aircraft altitude above 10000 m), coming from stratospheric air masses which results in strong gradients for these two flights.

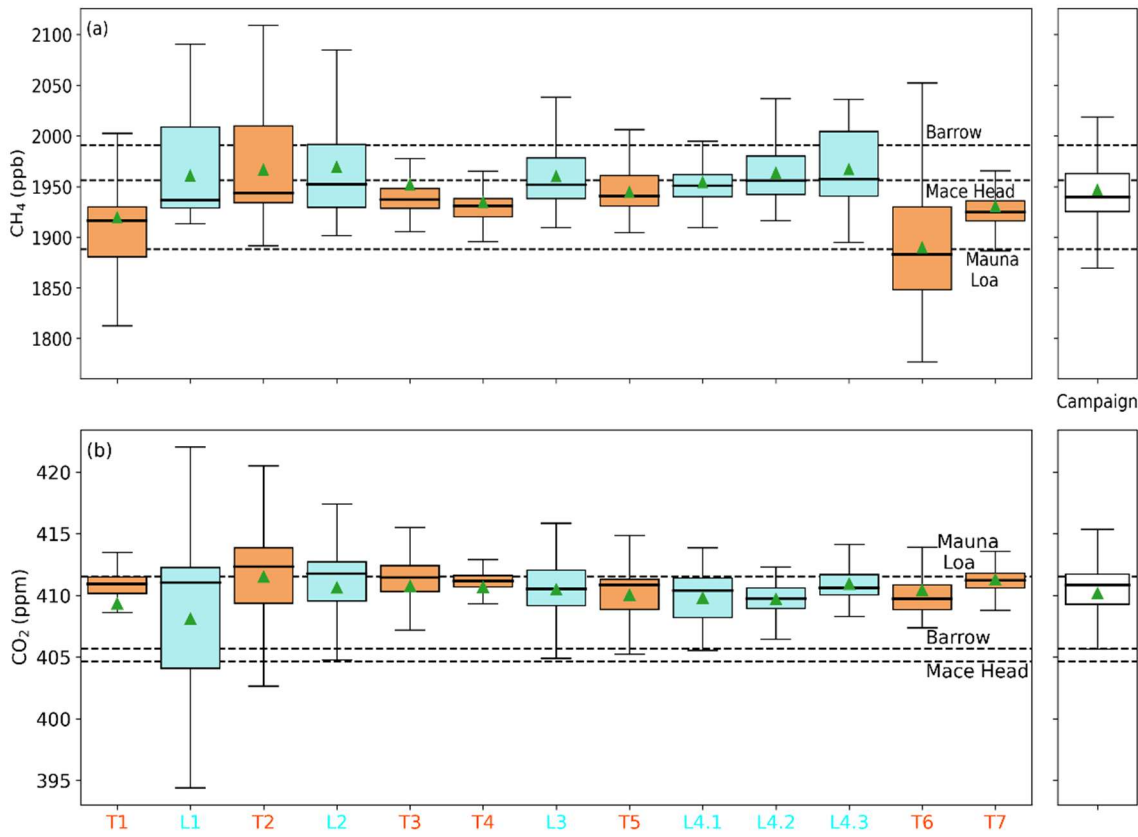


**Figure 4: (a) CH<sub>4</sub> mixing ratios variability by flight. Statistics for the entire campaign are shown in the right panel. The boxplot shows the interquartile range (25-75%) and the median value. The whiskers extend to the lowest and highest values, ignoring outliers beyond 1.5 times the interquartile range. Flight means are shown as green triangle. Dashed lines show respectively the mean monthly mixing ratios at Mauna Loa and Mace Head marine sector during September 2020. (b) Same as (a) for CO<sub>2</sub>.**

Generally, loop flights exhibit a higher first quartile than transit flights for low altitude values. These specific flights have indeed longer low-altitude legs and overall more frequent passages at low altitude (three ascent and descent for loops versus one ascent and one descent only for transits).

### 3.1.2 CO<sub>2</sub> mixing ratios

The average CO<sub>2</sub> mixing ratio of the campaign is 410.17±3.29 ppm, slightly below the seasonal average at Mauna Loa (411.52 ppm) but higher than Mace Head marine sector and Barrow values (respectively 404.62 ppm and 405.67 ppm). Figure 4b

presents the mixing ratio statistics for each flight and the whole campaign. Almost all median values are below the Mauna Loa reference, suggesting that air masses observed during the campaign may have intersected with regional CO<sub>2</sub> sinks. Candidate areas potentially explaining the sink include all terrestrial biomes in Russia (Bartalev et al., 2003; Belikov et al., 2019; Petäjä et al., 2021). Flight T1 flying over the Western Siberian taiga exhibits median values at low and high altitude respectively of 397.73 ppm and 410.92 ppm (with standard deviation of 4.30 ppm), highlighting the influence of these sinks. This biospheric uptake by Siberian boreal ecosystems (> 50° N) has already been observed during previous YAK-Aerosib campaigns realized in late-August or early-September. Vertical profiles for western flights at this time of the year present low CO<sub>2</sub> concentrations close to the surface jointly with a positive strong gradient when the altitude is increasing (Paris et al., 2008; Paris et al., 2010a). Paris et al. (2010b) demonstrated based on the relation between measured CO<sub>2</sub> concentration and airmasses' residence time in the lowest 300 m that for September campaign, the longer the airmasses resided over local areas (boreal and sub-arctic Siberia, > 50° N), the stronger the CO<sub>2</sub> uptake by Siberian ecosystems.

Two flights (L1 and T2) exhibit a large variability compared to the rest. For both flights, there are considerable gradients in CO<sub>2</sub> mixing ratios (+15 ppm and +10 ppm for respectively L1 and T2) between high and low altitudes suggesting the presence of effective sinks (forests and oceans in this case) at low altitude and the presence of "polluted" air masses at high altitude from long-range transport.

The highest mixing ratio measured during the campaign (451.85 ppm) was registered at the end of flight T6 while the aircraft was landing at the airport of Yakutsk. This is most likely driven by local pollution. At the time of landing the airport was fogged in (the aircraft was landed with difficulty due to the absence of enough fuel for flying to an alternate airfield).

290

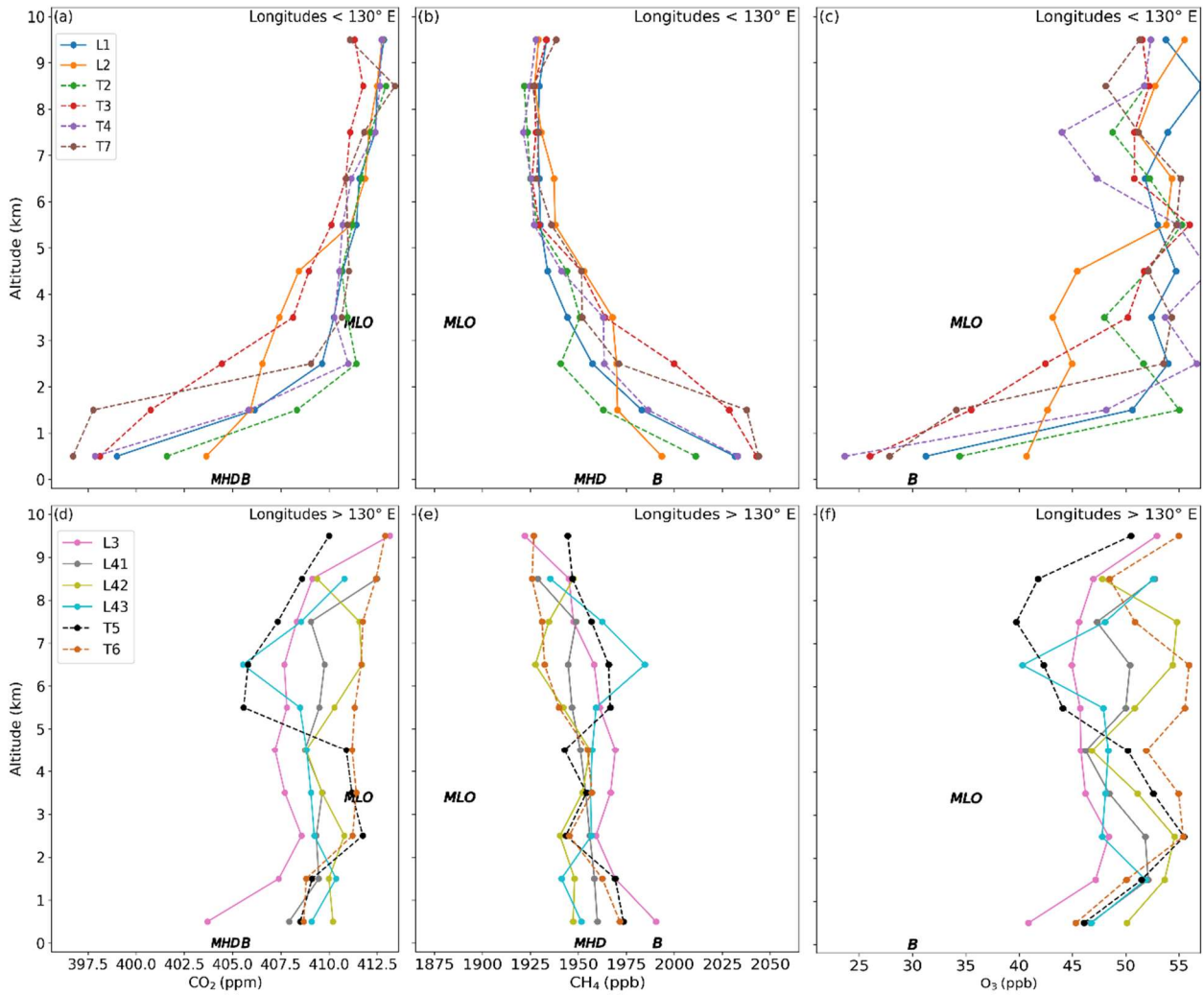
### 3.1.3 Comparing CO<sub>2</sub> and CH<sub>4</sub> variabilities

When comparing CO<sub>2</sub> and CH<sub>4</sub> profiles, two different types of flights appear: 1) both CO<sub>2</sub> and CH<sub>4</sub> present high variability such as in flights T2, L1, L2 or L3 illustrating active regional sources for both species and a strong uptake for CO<sub>2</sub>. 2) CH<sub>4</sub> present high variability (with relatively low values) while CO<sub>2</sub> is steady such as in flights T1 and T6. For CH<sub>4</sub>, it illustrates the influences of strong regional emissions for the highest values and of influx of stratospheric air for the lowest values. The CO<sub>2</sub> measured is subject to an attenuated vertical propagation of seasonal surface fluxes as demonstrated in Gerbig et al. (2003) leading to this relatively smaller variability during mostly high-altitude transit flights. To put these limited observations on the greenhouse gas variability in perspective, the following section discusses vertical distribution of mixing ratios.

### 3.2 Average vertical distribution of the gases

All data were binned every 1000 m in a range of ±500 m to get vertical profiles in Fig. 5. Data were also stratified according to their longitude, separating regions West and East of the 130° E meridian. As reported in Sect. 3.1, western flights exhibit

large vertical gradient in mean gas mixing ratios (high minus low altitude means ranging between -64 to -109 ppb, +9.10 to +14.80 ppm and -14 to -29 ppb respectively for CH<sub>4</sub>, CO<sub>2</sub>, and O<sub>3</sub>) compared to eastern flights.



305 **Figure 5: Flight mean vertical mixing ratio profiles for CO<sub>2</sub> (a, d), CH<sub>4</sub> (b, e), and O<sub>3</sub> (c, f). Top row shows flights West of 130°E while bottom row shows flights East of 130° E. Flight T1 is not shown due to missing data. Monthly mean values at Mauna Loa (MLO), Mace Head marine sector (MHD) and Barrow (B) in September 2020 are shown in each panel.**

310 For CH<sub>4</sub> at low altitude, western flights (Fig. 5b) present higher mixing ratios than eastern flights (Fig. 5e) with the biggest values in T3 and T7, closely followed by L1 and T4. Another feature of western flights is the difference of gradient between low and high altitudes: all western flights except L2 have a much steeper gradient between 0 and 3000 m (ranging from -74 ppb for L1 to -42 ppb for T3 with increasing altitude) than between 3000 and 10000 m (ranging from +11 ppb for L1 to +38 ppb for L2 with increasing altitude). Combining this information with the observation of the biggest CH<sub>4</sub> mixing ratio close to

the ground indicates a strong local source that are the Ural wetlands as reported in Belikov et al. (2019). At high altitude, no  
315 conclusion on the origin of the influences can be made at this moment. This will be investigated in Sect. 3.4.1 using the  
simulated CH<sub>4</sub> enhancements and the footprints. On the opposite, low altitude values for eastern flights (Fig. 5e) are  
encompassed in a range between 1947 ppb and 1990 ppb. These mixing ratios still represent an enhancement of +60 ppb to +  
100 ppb compared to the hemispheric reference (Mauna Loa monthly mean) of 1888 ppb. The references of Mace Head marine  
sector and Barrow respectively at 1956 ppb and 1991 ppb are in the same range as the easternmost flights' low altitude values  
320 but below western flights low altitude values. The simulated enhancements presented in Sect. 3.4.1 are also necessary to  
identify the sources at the origin of the CH<sub>4</sub> measured here. For flights T5 and L4.3, a layer of elevated CH<sub>4</sub> mixing ratios is  
crossed in the mid troposphere between approximately 6 and 8 km altitude (Fig. 5e). In Flight L4.3, for example, the vertical  
CH<sub>4</sub> gradient represents an excess of ~20 ppb between 6500 m and 8500 m compared to the underlying layer (between 4500  
m and 6500 m). This increase of CH<sub>4</sub> at top altitudes for flight L4.3 correlates with a decrease of O<sub>3</sub> mixing ratio of -10 ppb  
325 between 7500 m and 8500 m and a decrease in CO<sub>2</sub>. The possible origin of this high-altitude O<sub>3</sub> depletion will be investigated  
in Sect. 3.3.1 using individual vertical profiles that exhibit the same distribution for other flights such as L3 (also T4 or L2 not  
shown in the study).

O<sub>3</sub> vertical profiles generally increase with altitude, especially in the western flights, and follow a trend opposite to that of CH<sub>4</sub>  
mixing ratios. Eastern flights present an enhancement of +10 ppb to +20 ppb as compared to respective Mauna Loa and Barrow  
330 mixing ratios of 35 ppb and 30 ppb for the same altitude range, while western mixing ratios agree with the value from Barrow  
but above the one from Mauna Loa. O<sub>3</sub> and CH<sub>4</sub> measurements are above the corresponding reference values and therefore  
reflect regional variability of transport that need deeper investigation.

For CO<sub>2</sub>, our measurements are comparable to the Mauna Loa monthly mean (411.52 ppm) in the free tropospheric altitude  
range of the site (2000-3000 m). Mean CO<sub>2</sub> measured during the western flights in the lowest 1000 m (397-403 ppm) is  
335 consistently lower than Mace Head marine sector and Barrow monthly means (respectively 404.62 ppm and 405.67 ppm). As  
for CH<sub>4</sub>, all western CO<sub>2</sub> vertical profiles (except for L2) have a steeper gradient between 0 and 3000 m (ranging from 6.3  
ppm for T3 to 13.1 ppm for T4 with increasing altitude) than between 3000 and 10000 m (ranging from 0.4 ppm for T7 to 3.2  
ppm for T3 with increasing altitude) conjointly supporting the inference made in Sect. 3.1.2 on the strong uptake by Siberian  
ecosystems. On the opposite, eastern flights except L3 present mean CO<sub>2</sub> mixing ratios below 1000 m higher than Mace Head  
340 marine sector and Barrow means. The four highest mean CO<sub>2</sub> mixing ratios close to the ground are collected during eastern  
profiles (Fig. 5d). These are the three loops of Bering Strait and the transit T6 landing at Yakutsk. For flight T6, half of the  
low altitude values were taken in the vicinity of the city of Yakutsk and could be subject to local pollution. Concerning the  
city of Yakutsk, CH<sub>4</sub> also presents high mixing ratios at low altitudes with values of 1972 ppb and 2045 ppb for respective  
flights T6 and T7. Highest average mixing ratios at low altitudes for CO are also measured during flights T6 and T7 with  
345 similar values of 103 ppb and 107 ppb respectively. The loops L4.1, L4.2 and L4.3 in remote marine environments will be

investigated in Sect. 3.2.2. Flights L4.3 and T5 present a lower CO<sub>2</sub> layer at higher altitude (respectively 6500 m and 5500 m) already noted previously.

These observations show that the atmosphere over Siberia is affected by a complex pattern of influences from local emissions and long-range transport of polluted air masses. It highlights the importance of untangling the different influences on atmospheric composition (Petäjä et al., 2021) that will be further discussed in the next section.

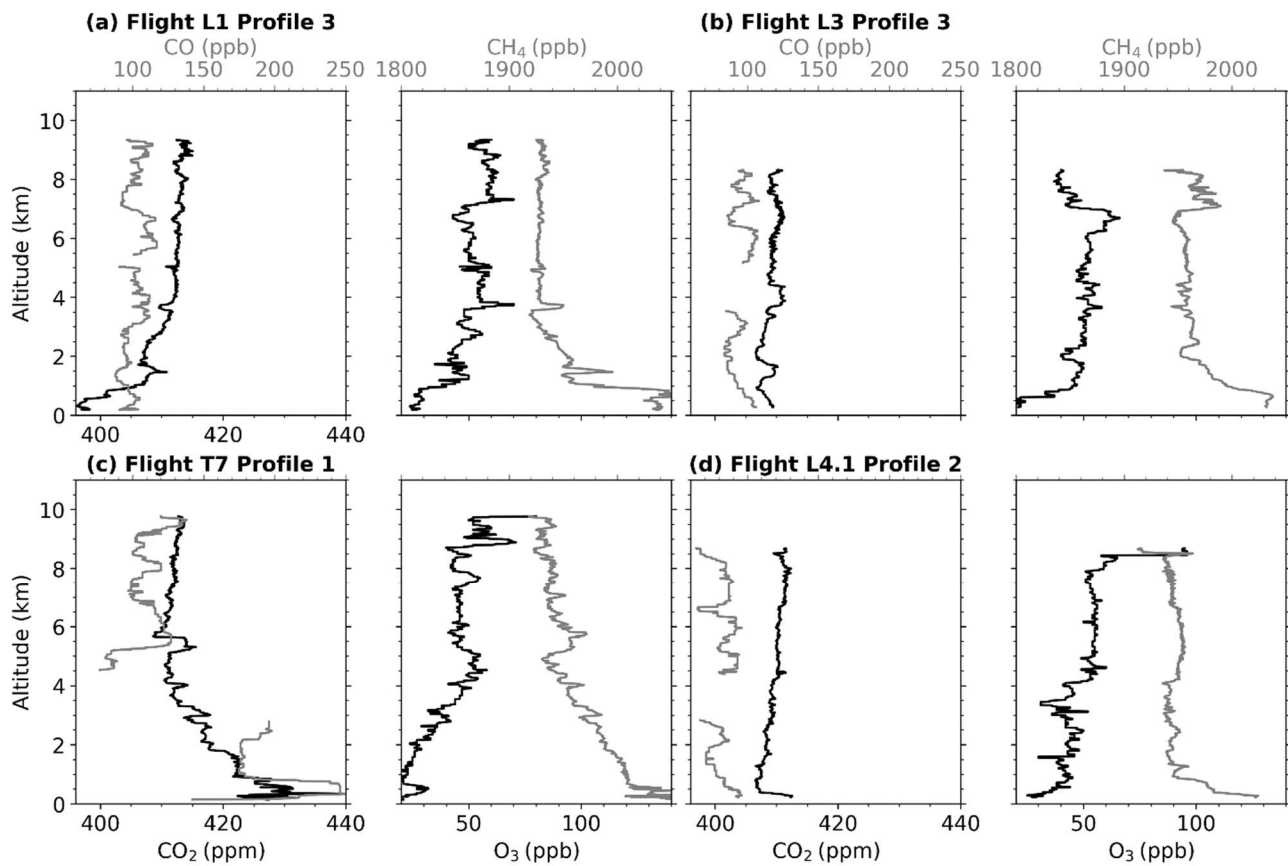
### 3.3 Individual vertical profiles and regional atmospheric transport

#### 3.3.1 North-Western Russia

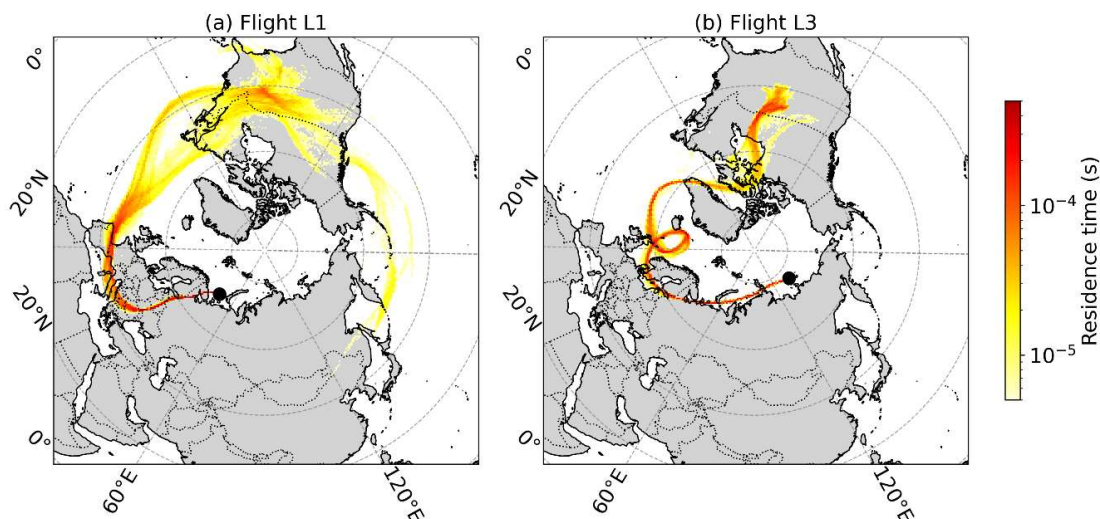
Figure 6 displays four selected profiles (either ascent or descent) that are representative of vertical distribution of trace gases mixing ratios encountered during the campaign. Figure 6a is a profile of flight L1 characterized by taiga and wetland environments. The flight L1 was highlighted in Sect. 3.1.1. for having the largest CO<sub>2</sub> interquartile range of the whole campaign. Fig. 6b is a profile of flight L3 close to the ESAS. Fig 6c shows a profile of flight T7 crossing the city of Yakutsk in regions covered by forests of coniferous trees and agricultural lands, and Fig. 6d represents a profile of flight L4.1 located near the Bering straits in biomes such as Arctic deserts, tundra, and forest tundra.

The vertical profile shown in Fig. 6a presents a large CO<sub>2</sub> depletion of 14 ppm in the lowest 2000 m depth layer, highlighting the strong drawdown of CO<sub>2</sub> in BL air. Higher altitude air corresponds to free tropospheric air masses that mostly resided over western European countries and United States to finally arrive in Russia from high altitudes (see footprint in Fig. 7a). These regions are important CO<sub>2</sub> and CH<sub>4</sub> emitters through fossil fuel exploitation and combustion, agriculture and waste management as documented in the EDGAR inventories (Crippa et al., 2019). This shows that the tropospheric air over the area of flight L1 is dominated by the outflow of European BL air interplaying with CO<sub>2</sub> uptake in the BL. Both CH<sub>4</sub> and O<sub>3</sub> profiles present an inversion corresponding to a “chemical” BL around 1000 m (with gradients respectively -90 ppb and +25 ppb). Below 3000 m, CH<sub>4</sub> is anti-correlated with O<sub>3</sub> while the two gases present common features above this altitude, with thin positively correlated layers at 4000 m and 5000 m.





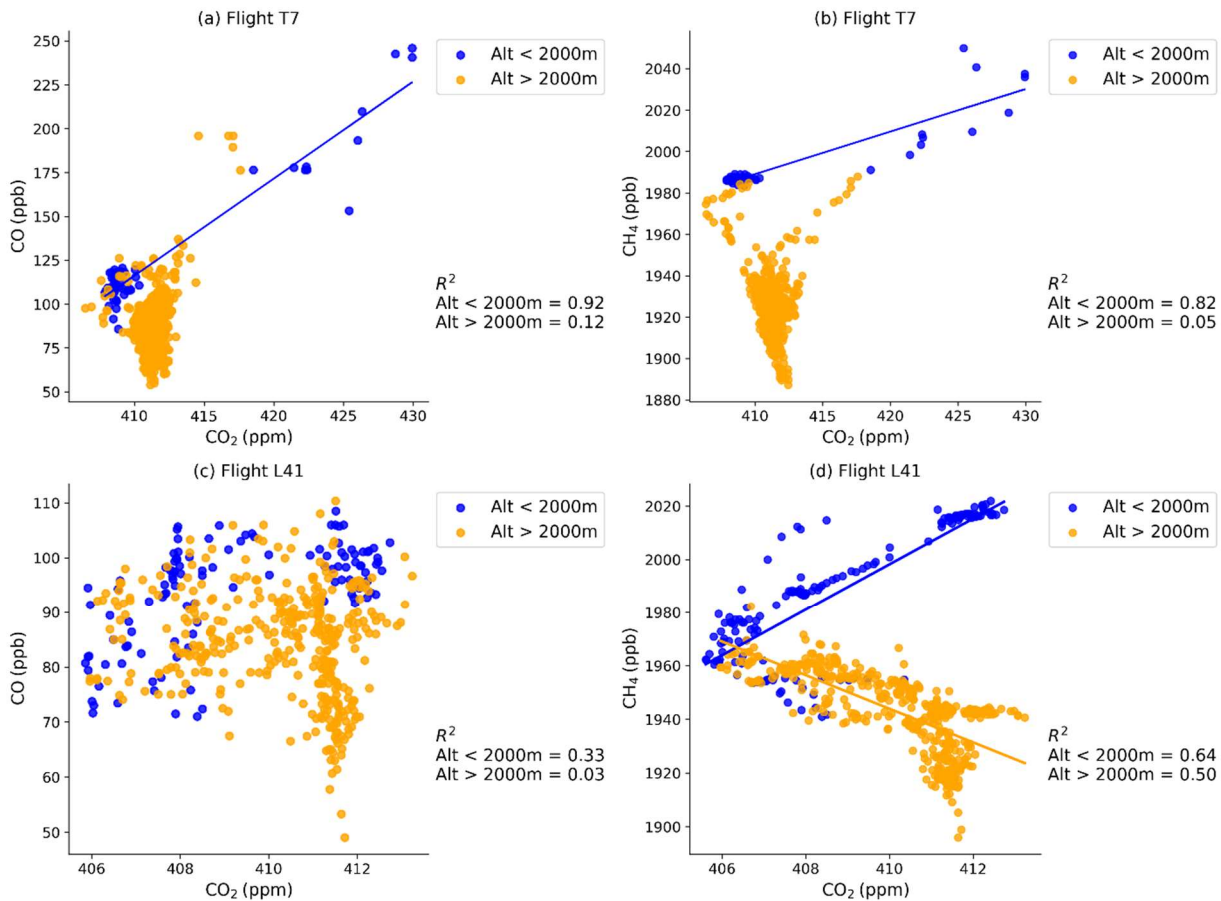
370 **Figure 6: Four selected vertical profiles of the campaign. CO<sub>2</sub> and CO are respectively in black and gray on each left plot. O<sub>3</sub> and CH<sub>4</sub> are respectively in black and gray on each right plot.**



375 **Figure 7: Total column footprints for simulated retro-transport of particles released at 14:53 UTC at an altitude of 9324 m during flight L1 (a) and at 05:01 UTC at an altitude of 5256 m during flight L3 (b). The black dot represents the receptor position.**

Figure 6b shows the second ascent of L3, in the North of Siberia. Here, CO<sub>2</sub> mixing ratio shows less variability than flight L1 profile 3. A slight decrease of -3 ppm of CO<sub>2</sub> and -20 ppb of CO with altitude can be observed under 1000 m, possibly  
 380 indicating the influence of emissions by local combustion, although this ascent does not start at an airport. We can also observe a stratification in the CO<sub>2</sub> and CO profiles with mixing ratio changes in stacked layers whose thickness vary between 500 m and 1500 m. This stratification has already been observed in previous campaigns (Paris et al. 2008) and is due to slow stirring in the troposphere under reduced vertical mixing. This profile is also characterized by significant sources of CH<sub>4</sub> in the BL as it is suggested by the strong enhancement of 100 ppb close to the ground (Fig. 6b). Among potential sources is methane  
 385 hydrates degradation from the East Siberian Arctic Shelf (Berchet et al., 2016; Thornton et al., 2016; Berchet et al., 2020). The influence of potential sources will be discussed in Sect 3.4. In the same profile, O<sub>3</sub> is anti-correlated with CH<sub>4</sub> above 3000 m, except at the top altitude around 8500 m where O<sub>3</sub> mixing ratios unexpectedly decrease closer to the stratosphere. This O<sub>3</sub> depletion mentioned in Sect 3.2. (-24 ppb compared to immediately lower layers) occurs in the air mass whose history is shown in Fig 7b. The same backward transport simulation with a threshold altitude of 500 m (appendix Fig. C1) shows an air mass  
 390 coming from the BL in Northern America then crossing the Atlantic Ocean and Northern Europe (only visible on the total column footprint). This layer with poor ozone mixing ratio is likely to be an uplift of BL air with the origin of the depletion potentially coming from another location further upstream. The O<sub>3</sub> mixing ratio at top altitude varies from 37 to 40 ppb which is comparable to local mixing ratio at 2000 m (40 to 42 ppb) of the same flight, or flight L1 (41 to 42 ppb just under 2000 m) corresponding to regional BL air.

Another singular event formerly mentioned was a possible pollution enhancement in the area of Yakutsk. The corresponding vertical profile in Fig. 6c shows high CO<sub>2</sub>, CH<sub>4</sub> and CO mixing ratios (respectively 439.60 ppm, 2070 ppb and 251 ppb) as the aircraft took off from Yakutsk. At low altitude, both CO and CH<sub>4</sub> present high correlation with CO<sub>2</sub> (respectively  $R^2 = 0.92$  and  $R^2 = 0.84$ ) as shown in Fig. 8a and Fig. 8b while there is no correlation at higher altitude. Such suggests combustion emissions possibly related to fossil fuel exploitation and/or use. This region is indeed characterized by the presence of operating O&G infrastructures and coal mines (Fig. 1). We can also observe the lowest O<sub>3</sub> mixing ratio of the campaign at 2 ppb at the ground level of Yakutsk (value too low to be seen on the figure). Having this O<sub>3</sub> near-ground minima over landing air-strips in polluted city plumes of Yakutsk suggests a titration of O<sub>3</sub> by NO.



405 **Figure 8:** Scatter plots of CO<sub>2</sub> vs CO (a) and CO<sub>2</sub> vs CH<sub>4</sub> (b) for flight T7. Same for flight L4.1 in (c) and (d). Blue dots and respective regression lines are for data acquired under 2000 m. Orange dots and respective regression lines are for data acquired above 2000 m. Correlation coefficient  $R^2$  are a displayed for each set.

### 3.3.3 CO<sub>2</sub> enhancement at low altitude in the Far East

410 Although the average CO<sub>2</sub> profiles of Flights L4.1, L4.2 and L4.3 show little variability over the Bering Strait we find significant CO<sub>2</sub> enhancements at very low altitude (<500m; Sect. 3.2). Here we focus our analysis on the loop L4.1 as the three flights have similar features. In the vertical profile of the first descent (second profile), remote from any airport, a high CO<sub>2</sub> mixing ratio of 412.5 ppm has been observed close to the surface (200m), against 407 ppm at 500 m altitude (Fig. 6d). The CH<sub>4</sub> mixing ratio also decreases from 2025 ppb to 1980 ppb between 200 m and 500 m altitude. On the other hand, CO presents  
415 only a small, opposite gradient of about -10 ppb across the same altitude range. Above 500m, the CO<sub>2</sub> profile exhibits a more typical shape of marginally increasing vertical gradient.

Figure 8c shows a scatter plot of CO against CO<sub>2</sub> for the whole flight L4.1 (including all six profiles). The correlation coefficient under 2000 m is significant but slightly lower ( $R^2 = 0.33$ ,  $p = 10^{-11}$ ) than correlation coefficients between CO<sub>2</sub> and CH<sub>4</sub> shown on Fig. 8d ( $R^2 = 0.64$ ,  $p = 10^{-37}$ ), suggesting that the CO<sub>2</sub> enhancement may be driven by a mixture of emissions  
420 including local combustion processes. The regression slope below 2000 m is 8.5 ppb of CH<sub>4</sub> per ppm of CO<sub>2</sub>. Non-combustion sources emitting both CO<sub>2</sub> and CH<sub>4</sub> leading to such signature could include one or several fossil fuel exploitation areas co-emitting the two species. According to the Global Fossil Infrastructure Tracker map from Global Monitor Energy, no operating O&G pipeline or terminal is reported in the East Siberian region, and the closest one being Kenai Alaska liquid natural gas terminal (Fig. 1). Still according to Global Energy Monitor, only Amaam North Coal Mine is active in East Siberian region  
425 (Fig. 1) but there are other coal mine activities reported in Russian Far East (Petäjä et al., 2021). Section 3.4.1 below shows that influence on this part of the flight L4.1 are mostly of natural origin and linked to the potential emission sensitivity of Alaskan emissions. Multiple regional and diffuse sources may be at play in explaining the enhancement observed. Another possibility is an emission from marine CH<sub>4</sub> sources. The absence of sea ice at the time of the campaign in the involved area (Fig. A1) (Fetterer et al., 2017) is enabling air-sea exchange, notably for CH<sub>4</sub>.

430 The anti-correlation between CO<sub>2</sub> and CH<sub>4</sub> above 2000 m (Fig. 8d) could be a residual from active sources for CH<sub>4</sub> and active sinks for CO<sub>2</sub> during the summer. While the air in this region has been relatively well-mixed as shown by the flat vertical profiles of CO<sub>2</sub> and CH<sub>4</sub> for flights L4.1, L4.2 and L4.3 (Fig. 5) and the reduced value ranges for CO<sub>2</sub> and CH<sub>4</sub> on the scatter plot of Fig. 8d (compared to the value ranges on Fig. 8b), mixing of airmasses affected simultaneously by CO<sub>2</sub> sinks and CH<sub>4</sub> sources in the past might be incomplete resulting in this residual anti-correlation. This will be better investigated in the Sect.  
435 3.4.1 by using the simulated mixing ratios for flight L4.1.

## 3.4 Untangling the different methane sources with a Lagrangian model

### 3.4.1 Contributions to measured CH<sub>4</sub> by source type and by location

This section aims at identifying the main emissions influencing the CH<sub>4</sub> mixing ratios through case studies of selected flights. Fig. 9 shows a scatter plot of measured and simulated CH<sub>4</sub> enhancements for each flight. Enhancement here refers to the

440 measured mixing ratio minus the background of the flight (background is defined in Sect. 2.3). Correlation coefficient  $R^2$  range  
between 0.28 (for flight T5) and 0.86 (for flight L1), with associated p-values that are inferior to  $10^{-10}$  for every flight. For  
most flights, the agreements between simulations and measurements are satisfactory and enable comparison of simulated  
source contributions to observed  $\text{CH}_4$  enhancements. However, the 1:1 dashed line highlights an underestimate of simulated  
mixing ratios that will be discussed in this section and the next one. For the study, we select one flight in western Siberia: T2  
445 that has a correlation coefficient  $R^2 = 0.82$ , and one flight in eastern Siberia: L4.1 that has a correlation coefficient  $R^2 = 0.67$ .

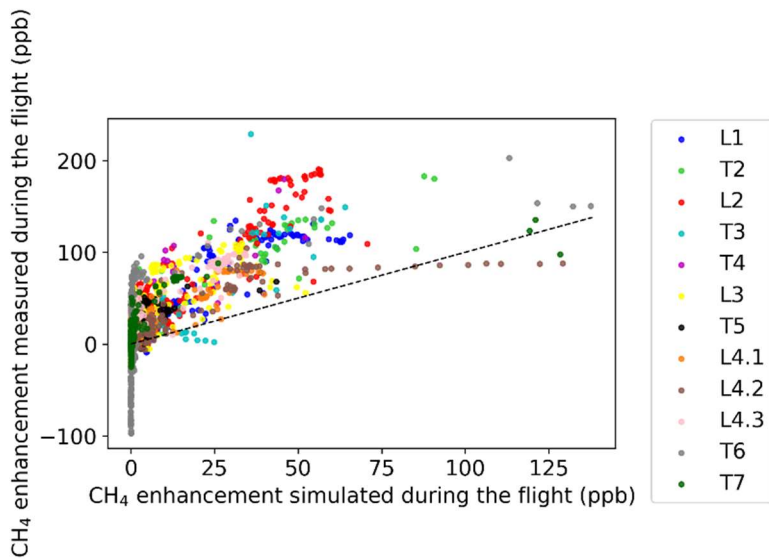
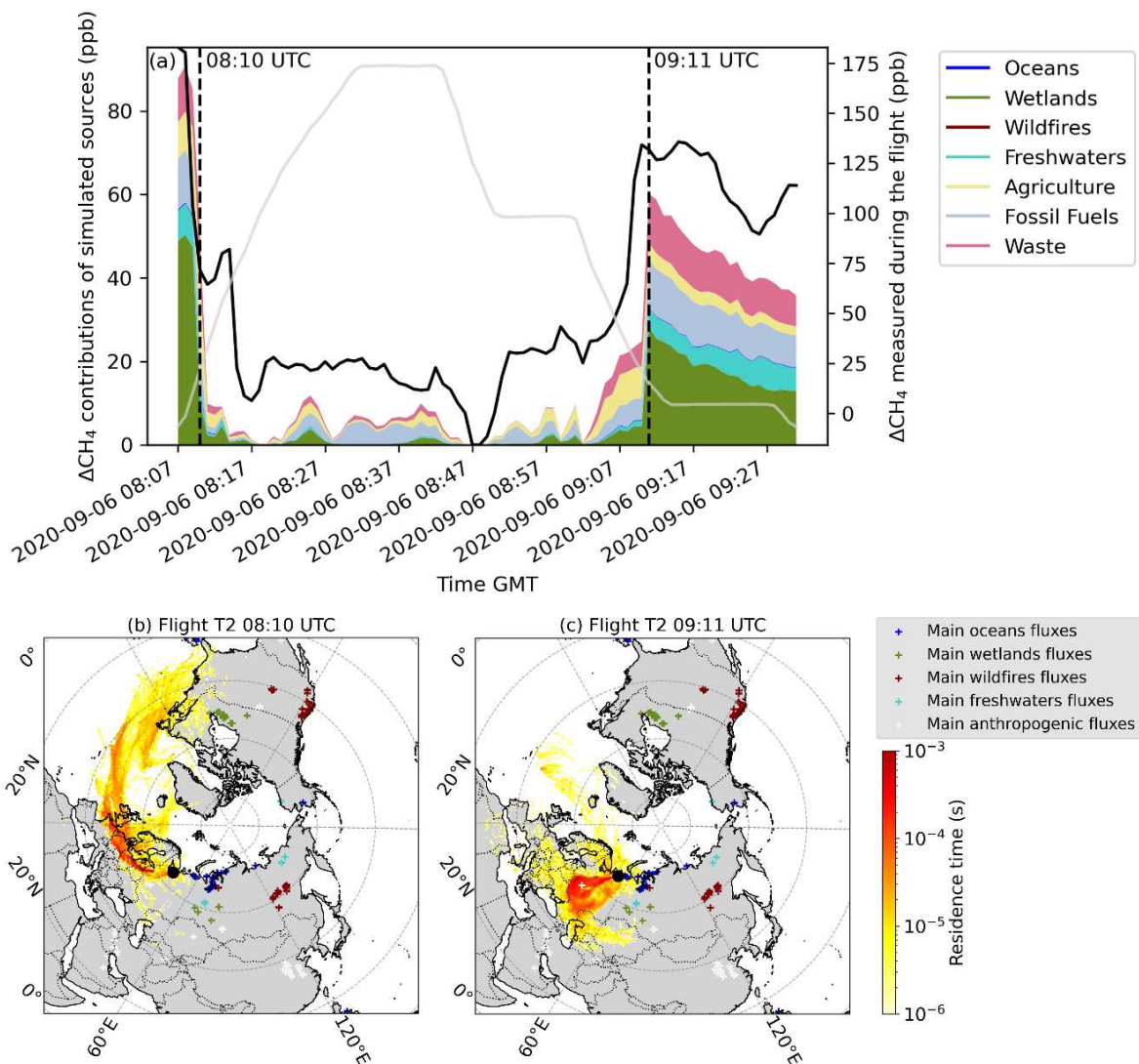


**Figure 9: Scatter plots of simulated  $\text{CH}_4$  enhancement vs measured  $\text{CH}_4$  for each flight of the campaign except T1 with the 1:1 black dashed line. Data were aggregated into 1 min bins to produce this figure.**

450 Figure 10 shows the simulated  $\text{CH}_4$  mixing ratios aggregating contributions from tagged sources during flight T2. The  
simulated signal at the receptor position is compared to measured  $\text{CH}_4$  enhancement. The  $\text{CH}_4$  enhancement variability is  
reasonably well reproduced by the model (Fig. 10a) but there is a consistent underestimation in total enhancement values. The  
possible reasons of this underestimate will be discussed later in Sect. 3.4.2. However, the ability of the model to reproduce the  
peaks and trough of  $\text{CH}_4$  during the entire campaign allows some confidence in the comparative tagged tracer analysis intended  
455 here.



460 **Figure 10: (a) Simulated  $\text{CH}_4$  enhancement (coloured stacked plot) and measured  $\text{CH}_4$  (black line) for flight T2. Note the different Y-axes. Altitude is shown in grey (bottom at 12 m and top at 8963 m). The two vertical dotted lines indicate the measurements represented in the following footprints. (b) 10 d potential emission sensitivity (PES) for particles released at 08:10 UTC. (c) Same as (b) at 09:11 UTC. The colored “+” symbols represent the fluxes with biggest intensities derived from each inventory. The black dot represents the receptor position.**

465 Figure 10b and c show PES for two selected positions representative for the flight. The footprint in Fig. 10b corresponds to the beginning of the ascent after leaving the airport (first dotted line at 08:10 UTC in panel a). At this position, an enhancement of 50 ppb was simulated. This enhancement is simulated to originate from a dominant anthropogenic contribution distributed between fossil fuel emissions, agriculture and waste management for a total of 36 ppb (the following highest contribution

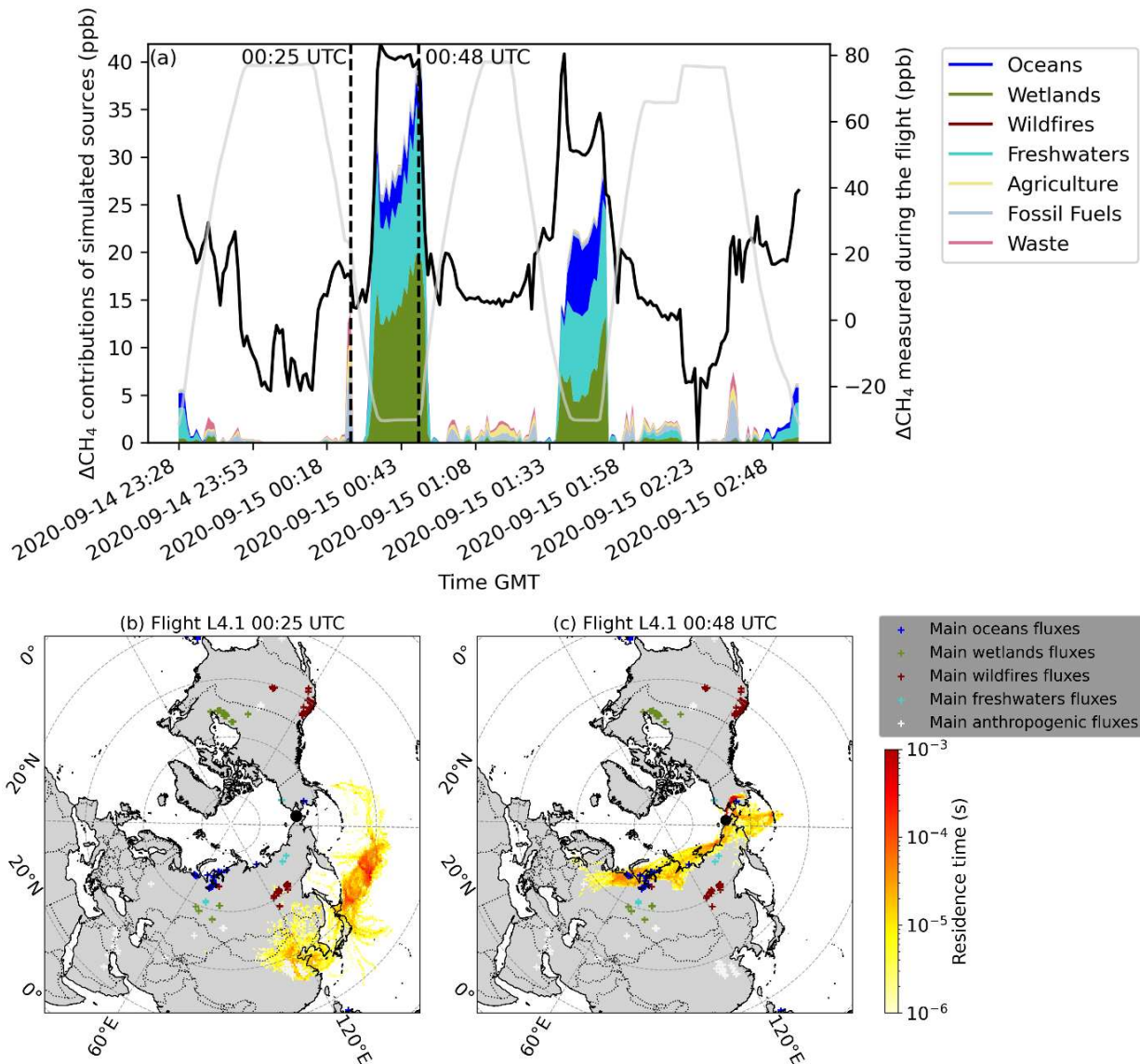
being wetlands with 10 ppb of contribution). The footprint Fig. 10b shows that the air mass has mostly resided over Western Russia, Central Europe, the Atlantic and, to a lesser extent USA (although this corresponds to an air mass age close to the limit of particle tracking of 10 days). This is consistent with the dominance of agricultural CH<sub>4</sub> fluxes in anthropogenic fluxes in Europe and the USA (appendix Fig. B1b) while agriculture is much less significant in the Russian emission inventories (Crippa et al., 2019). This documents long-range transport of free tropospheric air masses with relatively high CH<sub>4</sub> (comparable to values encountered in the BL) in western Siberia.

The footprint on Fig. 10c, close to the Arctic Ocean at lower altitude (second dotted line at 09:11 UTC in panel a), corresponds to mixed enhancements of 28 ppb by wetlands and 27 ppb by human activities. The PES is concentrated on western Russia, with a major sensitivity to anthropogenic flux at the core representing the city of Moscow (white-filled “plus” sign on Fig. 10c). The simulated enhancements are driven by with the CH<sub>4</sub> fluxes from fossil fuel exploitation and use (appendix Fig. B1a) in western Russia, and from wetland fluxes in Western Siberia (appendix Fig. B1c), especially in the Vasyugan swamp.

At the end of the flight, when getting closer to Naryan Mar, Fig. 10a depicts an enhancement of 7 ppb associated with freshwater sources that is represented by the constant light blue area between 09:11 UTC and the last data at 09:31 UTC. A large number of lakes are present around Naryan Mar and its surroundings (Fig. D1), supporting the importance of freshwater contribution in the atmospheric CH<sub>4</sub> burden. Also, it is likely that a part of the simulated enhancements due to wetlands may be associated to freshwater CH<sub>4</sub> emissions because there may be some overlap in inventories regarding small lakes and wetland sources, especially in complex regions with presence of many wetlands, lakes or rivers like in Naryan Mar outskirts.

Focusing now on Eastern Siberia, Fig. 11 illustrates the simulated and measured CH<sub>4</sub> enhancements, and two PES footprints associated with two specific positions of the flight. Overall, measured and simulated enhancements are lower than for the Western Siberian flight previously discussed. The first case (00:25 UTC during flight L4.1, first dotted line) is a very thin plume of elevated CH<sub>4</sub> in the lower free troposphere. It has a simulated enhancement of 14 ppb dominated by contributions due to fossil fuel emissions (7 ppb), agriculture (4 ppb) and waste management (3 ppb). The PES footprint in Fig. 11b shows that the air masses have partially resided over north-east China, very close to fossil fuel emission sources (see the white “+” sign on Fig. 11b) and where important CH<sub>4</sub> fluxes from agriculture are present (Fig. B1). Several fossil-fuel extraction infrastructures are located in this region (Global Energy Monitor, 2022). A large part of the air masses has also resided over East China Sea and Bering Strait where there are CH<sub>4</sub> fluxes due to offshore fossil fuel according to EDGAR inventories (appendix Fig. B1) explaining the domination of fossil fuel emission contribution in the selected peak. Overall at altitudes above 2000 m, most contributions are missed by the model showing that the air in the free troposphere has not been into contact with the surface for more than 10 days. This supports the anti-correlation observed in the Sect. 3.3.3 between CO<sub>2</sub> and CH<sub>4</sub> for flight 3.1 that is a residual of the active sources and sinks during the past summer.





500 **Figure 11: (a) Simulated  $\text{CH}_4$  enhancement (coloured stacked plot) and measured  $\text{CH}_4$  (black line) for flight L4.2. Note the different Y-axes. Altitude is shown in grey (bottom at 38 m and top at 8707 m). The two vertical dotted lines indicate the measurements represented in the following footprints. (b) 10 d potential emission sensitivity (PES) for particles released at 00:25 UTC. (c) Same as (b) at 00:48 UTC. The colored “+” symbols represent the fluxes with biggest intensities derived from each inventory. The black dot represents the receptor position.**

505 The second dotted line at 00:48 UTC in Fig. 11a is associated with simulated  $\text{CH}_4$  enhancement of 38ppb close to the BL. The simulation indicates that air masses travelled mostly over the Bering Strait, East Siberian Sea and Laptev Sea (Fig. 11c). The

enhancement is dominated (in relative terms) by the freshwater contribution with 15 ppb. Wetlands still play a large role with simulated mixing ratios that can represent 20% to 50% of the peaks at low altitude for this flight. Methane from the Arctic Ocean significantly appears in the simulated low-altitude enhancement but is lower than the other natural sources, with a maximum at 8 ppb in the same flight (Fig. 11a).

510 Over these two flights, we can observe that the peak-to-peak amplitude of simulated mixing ratios is higher than the peak-to-peak amplitude of measured mixing ratios indicating that some contributions are likely missing in our model (e.g. the second simulated peak of Fig. 10a, between 08:07 UTC and 08:17 UTC is missing some contributions). Some simulations though have smaller occurrences of underestimations of observed peaks, such as flight T3. Wildfires have influenced previous campaigns during specific episodes, especially close to the sources, as reported in Paris et al. (2008) and in Antokhin et al. 515 (2018). Here the wildfires are simulated as well, but are not visible since the contributions are negligible compared to the other ones over the whole campaign.

The contributions of the oceanic sources are not dominant in the simulation over any freshwater source in this study. Here, freshwaters appear as a dominant term in the CH<sub>4</sub> emitter influencing variability over Northern Siberia. Given the modelling uncertainties, it is challenging to attribute missing simulated CH<sub>4</sub> to a minor source term. Hence, comparing our simulated 520 and measured CH<sub>4</sub> time series do not provide sufficient confidence for assuming that the Weber et al. (2019) marine inventory is underestimated. The two PES footprints reveal a local CH<sub>4</sub> production in this part of Siberia, even in polluted air masses at high altitude whereas in the West they were resulting from long-range transport. In addition, there might be a sampling bias due to the campaign observation strategy. CH<sub>4</sub> measured from loops flights more often originates from natural sources compared to in transit flights, which sample BL air essentially in the vicinity of airports. The aircraft flies more frequently at 525 low altitude and over remote areas during the loop flights.

Overall, our model-data comparison indicated that CH<sub>4</sub> variability in Western Siberia is dominated by a combination of Western Siberia wetland sources and human activities largely related to fossil fuel emissions while eastern Siberia is characterized by strong natural sources such as wetlands, lakes, ponds and, to a smaller extent, oceans.

### 3.4.2 Sources of uncertainties and the underestimation of measurements

530 Although peaks and troughs are well simulated, total CH<sub>4</sub> mixing ratios across all flights were consistently underestimated. While FLEXPART is performing well at high altitudes in representing the signal variability, it has some limitations in simulating local pollution in the boundary layer. Stohl et al. (1995) reported that the representation of vertical transport leads to greater errors than lateral transport. This might be due either to the low resolution of meteorological data, poor emission inventory accuracy in Siberia, or a simplification of flux densities under the planetary boundary layer (Stohl et al., 1995). In 535 addition, the spatial resolution of 1° of the meteorological input data deteriorates the resolution of simulations under the planetary boundary layer.

Vertical transport across the boundary layer may have a significant role in the model underestimation given the trajectory of our aircraft campaign with large changes in altitude. Figure 12 shows the simulated CH<sub>4</sub> and measured enhancement for the period of the campaign at Barrow, Alaska (Dlugokencky et al., 2021c), which is obviously not subject to vertical movement of the receptor. Simulated mixing ratios are much less biased compared to the measurements (simulated mean CH<sub>4</sub> being at 52 ppb and Barrow CH<sub>4</sub> mean at 37 ppb). There are some occasional overestimates that might be due to fluxes included in both freshwater and wetland inventories. At this time of the year, Barrow is dominated by freshwater emissions from Alaska and Canada whereas anthropogenic emissions are largely absent in the simulation.

545

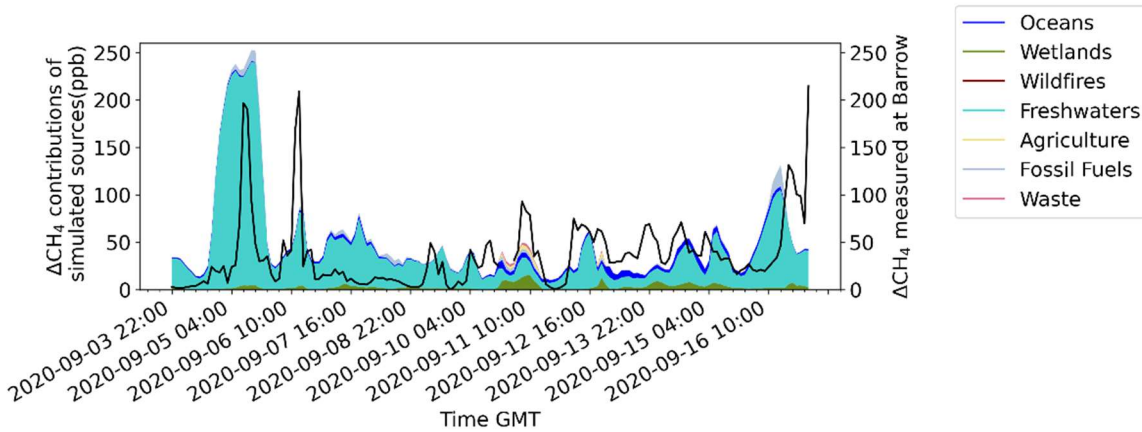


**Figure 12: Comparison of enhancement of measured CH<sub>4</sub> (black line) and simulated CH<sub>4</sub> (coloured stacked plot) at Barrow station during the whole campaign.**

550

For some inventories, the specific month of September 2020 was not available in the data. Previous years were used instead. This could lead to some underestimates as we can expect that emissions from some sources may possibly increase with time (e.g. CH<sub>4</sub> from anthropogenic activities) or subject to high temporal variability (CH<sub>4</sub> from natural biogenic sources). Two inventories, EDGAR (anthropogenic fluxes) and ORCHIDEE (fluxes from wetlands), were available for different years. We produced a sensitivity analysis by taking the previous years of these two inventories and producing the simulated mixing ratios for the same period. The time of reference is set to the month of September for the last year available of each inventory (2018 for EDGAR and 2017 for ORCHIDEE) and the mixing ratios of the two respective years before were also simulated. The simulations exhibited similar patterns, and we extracted the simulated values of the four peaks studied in Sect. 3.4.1. Enhancement's variations induced by changing the year of EDGAR inventories don't exceed 0.4 ppb. Enhancement's

560 variations induced by changing the year of ORCHIDEE inventories can go up to 5 ppb due to the variability of wetland emissions. This parameter ultimately appears to have little influence in our simulations that only cover a short period. Another source of error could be the underestimation of fluxes from poorly-known natural sources such as the marine ones. The estimation of CH<sub>4</sub> emissions by the ocean largely depends on the approach as reported in Weber et al. (2019). However, values vary significantly among the few available studies. For example, methane emissions in East Siberian Arctic Shelf are 565 still uncertain and are estimated to range between 8 and 17 Tg CH<sub>4</sub> yr<sup>-1</sup> (Berchet et al., 2016) by oceanographic approach, while an atmospheric inverse estimation provides a flux estimate not higher than 4.5 Tg CH<sub>4</sub> yr<sup>-1</sup> (Berchet et al., 2016). As discussed previously, they are influencing CH<sub>4</sub> variability but do not appear to be a dominant term in any part of our flights. Freshwater estimations are also subject to significant variability as it is difficult to be exhaustive in the distribution of the sources and there are fundamental gaps in the lakes model (Matthews et al., 2020). The “snapshot” effect of methane flux 570 measurements in field campaigns may also lead to underestimates (Wik et al., 2016) or biases. Further works may focus on performing simulations with other inventories such as the one used in Matthews et al. (2020) for high-latitude lakes or the submarine seep estimates from Etiope et al. (2019). On the other hand, it is reported in Matthews et al. (2020) that small wetlands are often interwoven with lakes causing difficulties to distinguish them which leads to overestimates. ORCHIDEE also may overestimate CH<sub>4</sub> net primary production by wetlands due to a lack of wetland specific plant functional types 575 representation (Ringeval et al., 2012; Wania et al., 2013). It could be relevant to test other flux estimated on wetlands and quantify the associated variation to check possible overestimates. The present study only captures a precise moment of the atmospheric condition in Siberia, giving an overview of main phenomena at the end of the summer in the year 2020. Therefore, observations should be completed with medium-term and long-term studies, and the aircraft data could be used as validation data for inverse modelling studies.

#### 580 **4 Conclusion**

We have investigated the latest data of September 2020 aircraft campaign over the Russia’s Arctic, including Siberia. It comprised 47 vertical profiles split in 13 flights across all of Siberia giving opportunities to observe CO<sub>2</sub> and CH<sub>4</sub> emissions and transport in different locations of an imperfectly known region that has a serious impact in global carbon budget. In-situ measurements of CO and O<sub>3</sub> have also been performed and are used as complementary tracers in this work. 585 CO<sub>2</sub> mixing ratios (median value of the campaign at 410.83±3.29 ppm) were slightly lower than Mauna Loa average (411.52 ppm) due to the passage of air masses above CO<sub>2</sub> sinks, and CH<sub>4</sub> mixing ratios (median value of the campaign at 1939±45 ppb) were higher (Mauna Loa average at 1888 ppb), indicating an accumulation of methane from different sources. Both gas show a high variability over Siberia, especially in the lower and the upper troposphere. Western Siberia exhibits steep mixing ratio gradients in CO<sub>2</sub> explained by the presence of effective sinks close to the ground (dense vegetation with taiga) while 590 higher altitudes are characterized by the long-range transport of air masses polluted by anthropogenic activities, mainly related to fossil fuel emissions. Eastern Siberia is subject to local pollution and CH<sub>4</sub> emissions from natural sources with less

atmospheric transport. Individual vertical profiles also revealed more unique patterns such as the stratification of CO<sub>2</sub> and CO mixing ratios with altitude, the O<sub>3</sub> depletion at top altitude in air masses that crossed Norwegian Sea, and the excess of CO<sub>2</sub> in Bering Strait region. As we wanted to determine if ocean fluxes (and hydrate gas) had a significant role in methane emissions, we simulated the CH<sub>4</sub> enhancement by different types of sources present in Siberia. It appeared that emissions are dominated by wetlands, fossil fuel emissions, agriculture and waste management in the West, and by freshwaters and wetlands in the East. Aquatic sources may be underestimated but our measurements are not sufficient to confront existing inventories due to limitations in the numerical models and observational strategy. However, our data suggests that poorly estimated aquatic emissions at regional scale in Arctic Siberia deserve further research and more measurements. With this insight on the main methane sources in northern Russia at the end of summer, we advocate for further research on aquatic CH<sub>4</sub> sources in Siberia to better predict potential positive feedbacks between regional and global warming.

**Data availability.** In flight measurement data is currently available from the authors upon request (at [jean-daniel.paris@lscce.ipsl.fr](mailto:jean-daniel.paris@lscce.ipsl.fr)). Data will be available online with access through: <https://yak.aeris-data.fr/>.

**Author contributions.** CN performed data processing and simulations, and analysed the data. JDP designed the study. CN and JDP wrote the first version of the manuscript. AB, SW and MS helped to perform simulations. BB, MA, and SB designed, organised and together with DD, AF, and AK performed the aircraft campaign and did the trace gas measurements. All contributed to the manuscript.

**Competing interests.** None

**Acknowledgements.** The aircraft campaign was realised by V.E. Zuev Institute of Atmospheric Optics SB RAS under the financial support of Ministry of Science and Higher Education of the Russian Federation (Agreement No. 075-15-2021-934). Data exchange and collaboration was done in the frame of the YAK-AEROSIB MoU. We thank the European Centre for Medium Range Weather Forecasts (ECMWF) for the provision of ERA-Interim reanalysis data, the FLEXPART development team for the provision of the FLEXPART 9.2 model version. We thank Joel Thanwerdas, and Thibaud Thonat for adapting the inventories used in the study. The MEMENTO database is administered by the Kiel Data Management Team at GEOMAR Helmholtz Centre for Ocean Research and supported by the German BMBF project SOPRAN (Surface Ocean Processes in the Anthropocene, <http://sopran.pangaea.de>). The database is accessible through the MEMENTO webpage: <https://memento.geomar.de>.

## References

- Antokhin, P. N., Arshinova, V. G., Arshinov, M. Y., Belan, B. D., Belan, S. B., Davydov, D. K., Ivlev, G. A., Fofonov, A. V., Kozlov, A. V., Paris, J. D., Nédélec, P., Rasskazchikova, T. M., Savkin, D. E., Simonenkov, D. V., Sklyadneva, T. K., and Tolmachev, G. N.: Distribution of Trace Gases and Aerosols in the Troposphere Over Siberia During Wildfires of Summer 2012, *J. Geophys. Res.-atmos.*, 123, 2285–2297, <https://doi.org/10.1002/2017JD026825>, 2018.
- Bartalev, S. A., Belward, A. S., Erchov, D. V., and Isaev, A. S.: A new SPOT4-VEGETATION derived land cover map of Northern Eurasia, *Int. J. of Remote. Sens.*, 24, 1977–1982, <https://doi.org/10.1080/0143116031000066297>, 2003.
- Belan, B. D., Ancellet, G., Andreeva, I. S., Antokhin, P. N., Arshinova, V. G., Arshinov, M. Y., Balin, Y. S., Barsuk, V. E., Belan, S. B., Chernov, D. G., Davydov, D. K., Fofonov, A. V., Ivlev, G. A., Kotelnikov, S. N., Kozlov, A. S., Kozlov, A. V., Law, K., Mikhail'chishin, A. V., Moseikin, I. A., Nasonov, S. V., Nédélec, P., Okhlopkova, O. V., Ol'kin, S. E., Panchenko, M. V., Paris, J.-D., Penner, I. E., Ptashnik, I. V., Rasskazchikova, T. M., Reznikova, I. K., Romanovskii, O. A., Safatov, A. S., Savkin, D. E., Simonenkov, D. V., Sklyadneva, T. K., Tolmachev, G. N., Yakovlev, S. V., and Zenkova, P. N.: Integrated airborne investigation of the air composition over the Russian sector of the Arctic, *Atmos. Meas. Tech.*, 15, 3941–3967, <https://doi.org/10.5194/amt-15-3941-2022>, 2022.
- Belikov, D., Arshinov, M., Belan, B., Davydov, D., Fofonov, A., Sasakawa, M., and Machida, T.: Analysis of the diurnal, weekly, and seasonal cycles and annual trends in atmospheric CO<sub>2</sub> and CH<sub>4</sub> at tower network in Siberia from 2005 to 2016, *Atmosphere-basel.*, 10, <https://doi.org/10.3390/atmos10110689>, 2019.
- Berchet, A., Paris, J. D., Ancellet, G., Law, K. S., Stohl, A., Nédélec, P., Arshinov, M. Y., Belan, B. D., and Ciais, P.: Tropospheric ozone over Siberia in spring 2010: Remote influences and stratospheric intrusion, *Tellus. B.*, 65, 1–14, <https://doi.org/10.3402/tellusb.v65i0.19688>, 2013.
- Berchet, A., Pison, I., Chevallier, F., Paris, J.-D., Bousquet, P., Bonne, J.-L., Arshinov, M. Y., Belan, B. D., Cressot, C., Davydov, D. K., Dlugokencky, E. J., Fofonov, A. V., Galanin, A., Lavrič, J., Machida, T., Parker, R., Sasakawa, M., Spahni, R., Stocker, B. D., and Winderlich, J.: Natural and anthropogenic methane fluxes in Eurasia: a mesoscale quantification by generalized atmospheric inversion, *Biogeosciences*, 12, 5393–5414, <https://doi.org/10.5194/bg-12-5393-2015>, 2015.
- Berchet, A., Bousquet, P., Pison, I., Locatelli, R., Chevallier, F., Paris, J. D., Dlugokencky, E. J., Laurila, T., Hatakka, J., Viisanen, Y., Worthy, D. E., Nisbet, E., Fisher, R., France, J., Lowry, D., Ivakhov, V., and Hermansen, O.: Atmospheric

constraints on the methane emissions from the East Siberian Shelf, *Atmos. Chem. Phys.*, 16, 4147–4157,  
655 <https://doi.org/10.5194/acp-16-4147-2016>, 2016.

Berchet, A., Pison, I., M. Crill, P., Thornton, B., Bousquet, P., Thonat, T., Hocking, T., Thanwerdas, J., Paris, J. D., and  
Saunois, M.: Using ship-borne observations of methane isotopic ratio in the Arctic Ocean to understand methane sources in  
the Arctic, *Atmos. Chem. Phys.*, 20, 3987–3998, <https://doi.org/10.5194/acp-20-3987-2020>, 2020.

660

Biraud S., Ciais P., Ramonet M., Simmonds P., Kazan V., Monfray P., O'Doherty S., Spain TG., Jennings SG.: European  
greenhouse gas emissions estimated from continuous atmospheric measurements and radon 222 at Mace Head, Ireland, *J.*  
*Geophys. Res-Atmos.*, 105, 1351-1366, <http://dx.doi.org/10.1029/1999JD900821>, 2000.

665 Ciais, P., Sabine, C., Govindasamy, B., Bopp, L., Brovkin, V., Canadell, J., Chhabra, A., DeFries, R., Galloway, J., Heimann,  
M., Jones, C., Le Quéré, C., Myneni, R., Piao, S., and Thornton, P.: Chapter 6: Carbon and Other Biogeochemical Cycles, in:  
*Climate Change 2013 The Physical Science Basis*, edited by: Stocker, T., Qin, D., and Plattner, G.-K., Cambridge University  
Press, Cambridge, 2013.

670 Crippa, M., Oreggioni, G., Guizzardi, D., Muntean, M., Schaaf, E., Lo Vullo, E., Solazzo, E., Monforti-Ferrario, F., Olivier,  
J., and Vignati, E.: Fossil CO<sub>2</sub> and GHG emissions of all world countries, Publications Office of the European Union,  
Luxembourg, <https://doi.org/doi:10.2760/687800>, 2019.

Dlugokencky, E., Mund, J., Crotwell, A., Crotwell, M., and Thoning, K.: Atmospheric Carbon Dioxide Dry Air Mole Frac-  
675 tions, NOAA GML Carbon Cycle Cooperative Global Air Sampling Network [data set],  
<https://doi.org/10.15138/wkgj-f215>, 2021a.

Dlugokencky, E., Mund, J., Crotwell, A., Crotwell, M., and Thoning, K.: Atmospheric Methane Dry Air Mole Fractions,  
NOAA GML Carbon Cycle Cooperative Global Air Sampling Network [data set],  
680 <https://doi.org/10.15138/wkgj-f215>, 2021b.

Dlugokencky, E., Mund, J., Crotwell, A., Crotwell, M., and Thoning, K.: Atmospheric methane from quasi-continuous  
measurements at Barrow, Alaska and Mauna Loa, Hawaii, 1986-2020, Version: 2021-03 [data set],  
<https://doi.org/10.15138/ve0c-be70>, 2021c.

685



- Elder, C. D., Thompson, D. R., Thorpe, A. K., Hanke, P., Walter Anthony, K. M., and Miller, C. E.: Airborne Mapping Reveals Emergent Power Law of Arctic Methane Emissions, *Geophys. Res. Lett.*, 47, <https://doi.org/10.1029/2019GL085707>, 2020.
- 690 Etiope, G., Ciotoli, G., Schwietzke, S., and Schoell, M.: Gridded maps of geological methane emissions and their isotopic signature, *Earth. Syst. Sci. Data.*, 11, 1–22, <https://doi.org/10.5194/essd-11-1-2019>, 2019.
- Etminan, M., Myhre, G., Highwood, E. J., and Shine, K. P.: Radiative forcing of carbon dioxide, methane, and nitrous oxide: A significant revision of the methane radiative forcing, *Geophys. Res. Lett.*, 43, <https://doi.org/10.1002/2016GL071930>, 2016.
- 695 Fetterer, F., Knowles, K., Meier, W. N., Savoie, M., and Windnagel, A. K.: Sea Ice Index, Version 3. [Sea Ice Extent], NSIDC: National Snow and Ice Data Center [data set], Sep 2020, <https://doi.org/https://doi.org/10.7265/N5K072F8>, 2017.
- Fleming, Z. L., Monks, P. S., and Manning, A. J.: Review: Untangling the influence of air-mass history in interpreting observed atmospheric composition, *Atmos. Res.*, 104-105, 1–39, <https://doi.org/10.1016/j.atmosres.2011.09.009>, 2012.
- 700 Friedlingstein, P., O’Sullivan, M., Jones, M. W., Andrew, R. M., Hauck, J., Olsen, A., Peters, G. P., Peters, W., Pongratz, J., Sitch, S., Le Quéré, C., Canadell, J. G., Ciais, P., Jackson, R. B., Alin, S., Aragão, L. E., Arneeth, A., Arora, V., Bates, N. R., Becker, M., Benoit-Cattin, A., Bittig, H. C., Bopp, L., Bultan, S., Chandra, N., Chevallier, F., Chini, L. P., Evans, W., Florentie, L., Forster, P. M., Gasser, T., Gehlen, M., Gilfillan, D., Gkritzalis, T., Gregor, L., Gruber, N., Harris, I., Hartung, K., Haverd, V., Houghton, R. A., Ilyina, T., Jain, A. K., Joetzjer, E., Kadono, K., Kato, E., Kitidis, V., Korsbakken, J. I., Landschützer, P., Lefèvre, N., Lenton, A., Lienert, S., Liu, Z., Lombardozzi, D., Marland, G., Metzl, N., Munro, D. R., Nabel, J. E., Nakaoka, S. I., Niwa, Y., O’Brien, K., Ono, T., Palmer, P. I., Pierrot, D., Poulter, B., Resplandy, L., Robertson, E., Rödenbeck, C., Schwinger, J., Séférian, R., Skjelvan, I., Smith, A. J., Sutton, A. J., Tanhua, T., Tans, P. P., Tian, H., Tilbrook, B., Van Der Werf, G., Vuichard, N., Walker, A. P., Wanninkhof, R., Watson, A. J., Willis, D., Wiltshire, A. J., Yuan, W., Yue, X., and Zaehle, S.: Global Carbon Budget 2020, *Earth. Syst. Sci. Data.*, 12, 3269–3340, <https://doi.org/10.5194/essd-12-3269-2020>, 2020.
- 705 Fujita, R., Morimoto, S., Maksyutov, S., Kim, H.-S., Arshinov, M., Brailsford, G., Aoki, S. and Nakazawa, T.: Global and Regional CH<sub>4</sub> Emissions for 1995–2013 Derived From Atmospheric CH<sub>4</sub>, δ<sup>13</sup>C-CH<sub>4</sub>, and δD-CH<sub>4</sub> Observations and a Chemical Transport Model. *J. Geophys. Res. Atmos.*, 125: e2020JD032903. <https://doi.org/10.1029/2020JD032903>, 2020.
- 715

Gerbig, C., Lin, J. C., Wofsy, S. C., Daube, B. C., Andrews, A. E., Stephens, B. B., Bakwin, P. S., and Grainger, C. A.: Toward constraining regional-scale fluxes of CO<sub>2</sub> with atmospheric observations over a continent: 2. Analysis of COBRA data using a receptor-oriented framework, *J. Geophys. Res.*, 108, 4757, doi:10.1029/2003JD003770, 2003.

720

“Global Coal Mine Tracker,” Global Energy Monitor: <https://globalenergymonitor.org/projects/global-coal-mine-tracker/> under the Creative Commons License <https://globalenergymonitor.org/creative-commons-public-license/>, last access: 19 September 2021, 2022.

725 “Global Fossil Infrastructure Tracker,” Global Energy Monitor: <https://globalenergymonitor.org/projects/global-fossil-infrastructure-tracker/tracker-map/> under the Creative Commons License <https://globalenergymonitor.org/creative-commons-public-license/>, last access: 19 September 2021, 2022.

Hazan, L., Tarniewicz, J., Ramonet, M., Laurent, O., and Abbaris, A.: Automatic processing of atmospheric CO<sub>2</sub> and CH<sub>4</sub> mole fractions at the ICOS Atmosphere Thematic Centre, *Atmos. Meas. Tech.*, 9, 4719-4736, <https://doi.org/doi:10.5194/amt-9-4719-2016>, 2016.

Hersbach, H., Bell, B., Berrisford, P., Biavati, G., Horányi, A., Muñoz Sabater, J., Nicolas, J., Peubey, C., Radu, R., Rozum, I., Schepers, D., Simmons, A., Soci, C., Dee, D., Thépaut, J.-N. (2018): ERA5 hourly data on single levels from 1979 to present, Copernicus Climate Change Service (C3S) Climate Data Store (CDS) [data set]. (Accessed on 04-10-2021), 10.24381/cds.adbb2d47, 2018.

Kirschke, S., Bousquet, P., Ciais, P., Saunois, M., Canadell, J. G., Dlugokencky, E. J., Bergamaschi, P., Bergmann, D., Blake, D. R., Bruhwiler, L., Cameron-Smith, P., Castaldi, S., Chevallier, F., Feng, L., Fraser, A., Heimann, M., Hodson, E. L., Houweling, S., Josse, B., Fraser, P. J., Krummel, P. B., Lamarque, J. F., Langenfelds, R. L., Le Quéré, C., Naik, V., O’doherly, S., Palmer, P. I., Pison, I., Plummer, D., Poulter, B., Prinn, R. G., Rigby, M., Ringeval, B., Santini, M., Schmidt, M., Shindell, D. T., Simpson, I. J., Spahni, R., Steele, L. P., Strode, S. A., Sudo, K., Szopa, S., Van Der Werf, G. R., Voulgarakis, A., Van Weele, M., Weiss, R. F., Williams, J. E., and Zeng, G.: Three decades of global methane sources and sinks, *Nat. Geosci.*, 6, 813–823, <https://doi.org/10.1038/ngeo1955>, 2013.

745

Kock, A. and Bange, H.: Counting the Ocean’s Greenhouse Gas Emissions, *Eos*, 96, <https://doi.org/10.1029/2015EO023665>, 2015.

Lan, X., Nisbet, E. G., Dlugokencky, E. J., and Michel, S. E.: What do we know about the global methane budget? Results

- 750 from four decades of atmospheric CH<sub>4</sub> observations and the way forward, *Philosophical Transactions of the Royal Society A: Mathematical, Physical and Engineering Sciences*, 379, 20200440, <https://doi.org/10.1098/rsta.2020.0440>, 2021.
- Lehner, B. and Döll, P.: Development and validation of a global database of lakes, reservoirs and wetlands, *J. Hydrol.*, 296, 1–22, <https://doi.org/10.1016/j.jhydrol.2004.03.028>, 2004.
- 755 Masson-Delmotte, V., Zhai, P., Pirani, A., Connors, S. L., Péan, C., Berger, S., Caud, N., Chen, Y., Goldfarb, L., Gomis, M. I., Huang, M., Leitzell, K., Lonnoy, E., Matthews, J. B. R., Maycock, T. K., Waterfield, T., Yelekçi, O., Yu, R., and Zhou, B. (Eds.): *Climate Change 2021: The Physical Science Basis. Contribution of Working Group I to the Sixth Assessment Report of the Intergovernmental Panel on Climate Change*, Cambridge University Press, Cambridge, 2021
- 760 Matthews, E., Johnson, M. S., Genovese, V., Du, J., and Bastviken, D.: Methane emission from high latitude lakes: methane-centric lake classification and satellite-driven annual cycle of emissions, *Sci. Rep.-uk.*, 10, 1–9, <https://doi.org/10.1038/s41598-020-68246-1>, 2020.
- 765 Melton, J. R., Wania, R., Hodson, E. L., Poulter, B., Ringeval, B., Spahni, R., Bohn, T., Avis, C. A., Beerling, D. J., Chen, G., Eliseev, A. V., Denisov, S. N., Hopcroft, P. O., Lettenmaier, D. P., Riley, W. J., Singarayer, J. S., Subin, Z. M., Tian, H., Zürcher, S., Brovkin, V., van Bodegom, P. M., Kleinen, T., Yu, Z. C., and Kaplan, J. O.: Present state of global wetland extent and wetland methane modelling: conclusions from a model inter-comparison project (WETCHIMP), *Biogeosciences*, 10, 753–788, <https://doi.org/10.5194/bg-10-753-2013>, 2013.
- 770 Oltmans, S. J. and Levy, H.: Surface ozone measurements from a global network, *Atmos. Environ.*, 28, 9–24, [https://doi.org/10.1016/1352-2310\(94\)90019-1](https://doi.org/10.1016/1352-2310(94)90019-1), 1994.
- Paris, J. D., Ciais, P., Nédélec, P., Ramonet, M., Belan, B. D., Arshinov, M. Y., Golitsyn, G. S., Granberg, I., Stohl, A., Cayez, G., Athier, G., Boumard, F., and Cousin, J. M.: The YAK-AEROSIB transcontinental aircraft campaigns: New insights on the transport of CO<sub>2</sub>, CO and O<sub>3</sub> across Siberia, *Tellus. B.*, 60, 551–568, <https://doi.org/10.1111/j.1600-0889.2008.00369.x>, 2008.
- Paris, J.-D., Stohl, A., Nédélec, P., Arshinov, M. Y., Panchenko, M. V., Shmargunov, V. P., Law, K. S., Belan, B. D., and Ciais, P.: Wildfire smoke in the Siberian Arctic in summer: source characterization and plume evolution from airborne measurements, *Atmos. Chem. Phys.*, 9, 9315–9327, <https://doi.org/10.5194/acp-9-9315-2009>, 2009.
- 780 Paris, J.-D., Ciais, P., Nédélec, P., Stohl, A., Belan, B. D., Arshinov, M. Y., Carouge, C., Golitsyn, G. S., and Granberg, I. G.:

New Insights on the Chemical Composition of the Siberian Air Shed From The Yak-Aerosib Aircraft Campaigns, *B. Am. Meteorol. Soc.*, 91, 625–642, <https://doi.org/10.1175/2009BAMS2663.1>, 2010a.

785

Paris, J.-D., Stohl, A., Ciais, P., Nédélec, P., Belan, B. D., Arshinov, M. Yu., and Ramonet, M.: Source-receptor relationships for airborne measurements of CO<sub>2</sub>, CO and O<sub>3</sub> above Siberia: a cluster-based approach, *Atmos. Chem. Phys.*, 10, 1671–1687, <https://doi.org/10.5194/acp-10-1671-2010>, 2010b.

790 Parmentier, F. J. W., Christensen, T. R., Rysgaard, S., Bendtsen, J., Glud, R. N., Else, B., van Huissteden, J., Sachs, T., Vonk, J. E., and Sejr, M. K.: A synthesis of the arctic terrestrial and marine carbon cycles under pressure from a dwindling cryosphere, *Ambio.*, 46, 53–69, <https://doi.org/10.1007/s13280-016-0872-8>, 2017.

795 Petäjä, T., Ganzei, K. S., Lappalainen, H. K., Tabakova, K., Makkonen, R., Räisänen, J., Chalov, S., Kulmala, M., Zilitinkevich, S., Baklanov, P. Y., Shakirov, R. B., Mishina, N. V., Egidarev, E. G., and Kondrat'ev, I. I.: Research agenda for the Russian Far East and utilization of multi-platform comprehensive environmental observations, *Int. J. Digit. Earth.*, 14, 311–337, <https://doi.org/10.1080/17538947.2020.1826589>, 2021.

800 Pisso, I., Sollum, E., Grythe, H., Kristiansen, N. I., Cassiani, M., Eckhardt, S., Arnold, D., Morton, D., Thompson, R. L., Groot Zwaafink, C. D., Evangelio, N., Sodemann, H., Haimberger, L., Henne, S., Brunner, D., Burkhart, J. F., Fouilloux, A., Brioude, J., Philipp, A., Seibert, P., and Stohl, A.: The Lagrangian particle dispersion model FLEXPART version 10.4, *Geosci. Model. Dev.*, 12, 4955–4997, <https://doi.org/10.5194/gmd-12-4955-2019>, 2019.

805 Platt, S., Eckhardt, S., Ferré, B., Fisher, R., Hermansen, O., Jansson, P., Lowry, D., Nisbet, E., Pisso, I., Schmidbauer, N., Silyakova, A., Stohl, A., Svendby, T., Vadakkepuliambatta, S., Mienert, J., and Lund Myhre, C.: Methane at svalbard and over the european arctic ocean, *Atmos. Chem. Phys.*, 18, 17 207–17 224, <https://doi.org/10.5194/acp-18-17207-2018>, 2018.

810 Reeves, C. E., Penkett, S. A., Bauguitte, S., Law, K. S., Evans, M. J., Bandy, B. J., Monks, P. S., Edwards, G. D., Phillips, G., Barjat, H., Kent, J., Dewey, K., Schmitgen, S., and Kley, D.: Potential for photochemical ozone formation in the troposphere over the North Atlantic as derived from aircraft observations during ACSOE, *Journal of Geophysical Research D: Atmospheres*, 107, <https://doi.org/10.1029/2002JD002415>, 2002.

815 Ringeval, B., Decharme, B., Piao, S. L., Ciais, P., Papa, F., de Noblet-Ducoudré, N., Prigent, C., Friedlingstein, P., Gouttevin, I., Koven, C., and Ducharme, A.: Modelling sub-grid wetland in the ORCHIDEE global land surface model: evaluation against river discharges and remotely sensed data, *Geosci. Model. Dev.*, 5, 941–962, <https://doi.org/10.5194/gmd-5-941-2012>, 2012.

Rosentreter, J. A., Borges, A. V., Deemer, B. R., Holgerson, M. A., Liu, S., Song, C., Melack, J., Raymond, P. A., Duarte, C. M., Allen, G. H., Olefeldt, D., Poulter, B., Battin, T. I., and Eyre, B. D.: Half of global methane emissions come from highly variable aquatic ecosystem sources, *Nat. Geosci.*, 14, 225–230, <https://doi.org/10.1038/s41561-021-00715-2>, 2021.

820

Ruppel, C.: Permafrost-Associated Gas Hydrate: Is It Really Approximately 1 % of the Global System?, *J. Chem. Eng. Data.*, 60, 429–436, <https://doi.org/10.1021/je500770m>, 2015.

Saunois, M., Bousquet, P., Poulter, B., Pregon, A., Ciais, P., Canadell, J. G., Dlugokencky, E. J., Etiope, G., Bastviken, D.,  
825 Houweling, S., Janssens-Maenhout, G., Tubiello, F. N., Castaldi, S., Jackson, R. B., Alexe, M., Arora, V. K., Beerling, D. J.,  
Bergamaschi, P., Blake, D. R., Brailsford, G., Brovkin, V., Bruhwiler, L., Crevoisier, C., Crill, P., Covey, K., Curry, C.,  
Frankenberg, C., Gedney, N., Höglund-Isaksson, L., Ishizawa, M., Ito, A., Joos, F., Kim, H.-S., Kleinen, T., Krummel, P.,  
Lamarque, J.-F., Langenfelds, R., Locatelli, R., Machida, T., Maksyutov, S., McDonald, K. C., Marshall, J., Melton, J. R.,  
Morino, I., Naik, V., O'Doherty, S., Parmentier, F.-J. W., Patra, P. K., Peng, C., Peng, S., Peters, G. P., Pison, I., Prigent, C.,  
830 Prinn, R., Ramonet, M., Riley, W. J., Saito, M., Santini, M., Schroeder, R., Simpson, I. J., Spahni, R., Steele, P., Takizawa,  
A., Thornton, B. F., Tian, H., Tohjima, Y., Viovy, N., Voulgarakis, A., van Weele, M., van der Werf, G. R., Weiss, R.,  
Wiedinmyer, C., Wilton, D. J., Wiltshire, A., Worthy, D., Wunch, D., Xu, X., Yoshida, Y., Zhang, B., Zhang, Z., and Zhu, Q.:  
The global methane budget 2000–2012, *Earth. Syst. Sci. Data.*, 8, 697–751, <https://doi.org/10.5194/essd-8-697-2016>, 2016.

835 Saunois, M., Stavert, A. R., Poulter, B., Bousquet, P., Canadell, J. G., Jackson, R. B., Raymond, P. A., Dlugokencky, E. J.,  
Houweling, S., Patra, P. K., Ciais, P., Arora, V. K., Bastviken, D., Bergamaschi, P., Blake, D. R., Brailsford, G., Bruhwiler,  
L., Carlson, K. M., Carrol, M., Castaldi, S., Chandra, N., Crevoisier, C., Crill, P. M., Covey, K., Curry, C. L., Etiope, G.,  
Frankenberg, C., Gedney, N., Hegglin, M. I., Höglund-Isaksson, L., Hugelius, G., Ishizawa, M., Ito, A., Janssens-Maenhout,  
G., Jensen, K. M., Joos, F., Kleinen, T., Krummel, P. B., Langenfelds, R. L., Laruelle, G. G., Liu, L., Machida, T., Maksyutov,  
840 S., McDonald, K. C., McNorton, J., Miller, P. A., Melton, J. R., Morino, I., Müller, J., Murguía-Flores, F., Naik, V., Niwa, Y.,  
Noce, S., O'Doherty, S., Parker, R. J., Peng, C., Peng, S., Peters, G. P., Prigent, C., Prinn, R., Ramonet, M., Regnier, P., Riley,  
W. J., Rosentreter, J. A., Segers, A., Simpson, I. J., Shi, H., Smith, S. J., Steele, L. P., Thornton, B. F., Tian, H., Tohjima, Y.,  
Tubiello, F. N., Tsuruta, A., Viovy, N., Voulgarakis, A., Weber, T. S., van Weele, M., van der Werf, G. R., Weiss, R. F.,  
Worthy, D., Wunch, D., Yin, Y., Yoshida, Y., Zhang, W., Zhang, Z., Zhao, Y., Zheng, B., Zhu, Q., Zhu, Q., and Zhuang, Q.:  
845 The Global Methane Budget 2000–2017, *Earth. Syst. Sci. Data.*, 12, 1561–1623, <https://doi.org/10.5194/essd-12-1561-2020>,  
2020.

- 850 Sasakawa, M., Shimoyama, K., Machida, T., Tsuda, N., Suto, H., Arshinov, M., Davydov, D., Fofonov, A., Krasnov, O., Saeki, T., Koyama, Y., and Maksyutov, S.: Continuous measurements of methane from a tower network over Siberia, *Tellus B: Chemical and Physical Meteorology*, 62:5, 403-416, DOI: 10.1111/j.1600-0889.2010.00494.x, 2010.
- 855 Sasakawa, M., Machida, T., Ishijima, K., Arshinov, M., Patra, P. K., Ito, A., Aoki, S., and Petrov, V.: Temporal characteristics of CH<sub>4</sub> vertical profiles observed in the West Siberian Lowland over Surgut from 1993 to 2015 and Novosibirsk from 1997 to 2015. *Journal of Geophysical Research: Atmospheres*, 122, 11,261– 11,273. <https://doi.org/10.1002/2017JD026836>, 2017.
- Seibert, P. and Frank, A.: Source-receptor matrix calculation with a Lagrangian particle dispersion model in backward mode, *Atmos. Chem. Phys.*, 4, 51–63, <https://doi.org/10.5194/acp-4-51-2004>, 2004.
- 860 Shakhova, N., Semiletov, I., Salyuk, A., Yusupov, V., Kosmach, D., and Gustafsson, O.: Extensive Methane Venting to the Atmosphere from Sediments of the East Siberian Arctic Shelf, *Science.*, 327, 1246–1250, <https://doi.org/10.1126/science.1182221>, 2010.
- 865 Skorokhod, A. I., Berezina, E. V., Moiseenko, K. B., Elansky, N. F., and Belikov, I. B.: Benzene and toluene in the surface air of northern Eurasia from TROICA-12 campaign along the Trans-Siberian Railway, *Atmos. Chem. Phys.*, 17, 5501–5514, <https://doi.org/10.5194/acp-17-5501-2017>, 2017.
- Stohl, A. and Thomson, D. J.: A Density Correction for Lagrangian Particle Dispersion Models, *Bound-Lay. Meteorol.*, 90, 155–167, <https://doi.org/10.1023/A:1001741110696>, 1999.
- 870 Stohl, A., Wotawa, G., Seibert, P., and Kromp-Kolb, H.: Interpolation Errors in Wind Fields as a Function of Spatial and Temporal Resolution and Their Impact on Different Types of Kinematic Trajectories, *J. Appl. Meteorol.*, 34, 2149–2165, [https://doi.org/10.1175/1520-0450\(1995\)034<2149:IEIWFA>2.0.CO;2](https://doi.org/10.1175/1520-0450(1995)034<2149:IEIWFA>2.0.CO;2), 1995.
- 875 Stohl, A., Hittenberger, M., and Wotawa, G.: Validation of the lagrangian particle dispersion model FLEXPART against large-scale tracer experiment data, *Atmos. Environ.*, 32, 4245–4264, [https://doi.org/10.1016/S13522310\(98\)00184\\_8](https://doi.org/10.1016/S13522310(98)00184_8), 1998.
- Stohl, A., Forster, C., Frank, A., Seibert, P., and Wotawa, G.: Technical note: The Lagrangian particle dispersion model FLEXPART version 6.2, *Atmos. Chem. Phys.*, 5, 2461–2474, <https://doi.org/10.5194/acp-5-2461-2005>, 2005.

- 880 Stöckli, R., Vermote, E., Saleous, N., Simmon, R., and Herring, D.: The Blue Marble Next Generation - A true color earth dataset including seasonal dynamics from MODIS., corresponding author: rstockli@climate.gsfc.nasa.gov.
- Tan, Z., Zhuang, Q., and Walter Anthony, K.: Modeling methane emissions from arctic lakes: Model development and site-level study, *J. Adv. Model. Earth. Sy.*, 7, 459–483, <https://doi.org/10.1002/2014MS000344>, 2015.
- 885 Thonat, T., Saunio, M., Bousquet, P., Pison, I., Tan, Z., Zhuang, Q., Crill, P. M., Thornton, B. F., Bastviken, D., Dlugokencky, E. J., Zimov, N., Laurila, T., Hatakka, J., Hermansen, O., and Worthy, D. E. J.: Detectability of Arctic methane sources at six sites performing continuous atmospheric measurements, *Atmos. Chem. Phys.*, 17, 8371–8394, <https://doi.org/10.5194/acp-17-8371-2017>, 2017
- 890 Thornton, B. F., Geibel, M. C., Crill, P. M., Humborg, C., and Mörrth, C. M.: Methane fluxes from the sea to the atmosphere across the Siberian shelf seas, *Geophys. Res. Lett.*, 43, 5869–5877, <https://doi.org/10.1002/2016GL068977>, 2016.
- Thornton, B. F., Prytherch, J., Andersson, K., Brooks, I. M., Salisbury, D., Tjernström, M., and Crill, P. M.: Shipborne eddy covariance observations of methane fluxes constrain Arctic sea emissions, *Sci. Adv.*, 6, 1–11, <https://doi.org/10.1126/sciadv.aay7934>, 2020.
- Turetsky, M. R., Jones, M., Walter Anthony, K., Olefeldt, D., Schuur, E. A., Koven, C., Mcguire, A. D., and Grosse, G.: Permafrost collapse is accelerating carbon release, *Nature.*, 569, 32–24, 2019.
- 900 van der Werf, G. R., Randerson, J. T., Giglio, L., van Leeuwen, T. T., Chen, Y., Rogers, B. M., Mu, M., van Marle, M. J. E., Morton, D. C., Collatz, G. J., Yokelson, R. J., and Kasibhatla, P. S.: Global fire emissions estimates during 1997–2016, *Earth. Syst. Sci. Data.*, 9, 697–720, <https://doi.org/10.5194/essd-9-697-2017>, 2017.
- 905 Wania, R., Melton, J. R., Hodson, E. L., Poulter, B., Ringeval, B., Spahni, R., Bohn, T., Avis, C. A., Chen, G., Eliseev, A. V., Hopcroft, P. O., Riley, W. J., Subin, Z. M., Tian, H., Van Bodegom, P. M., Kleinen, T., Yu, Z. C., Singarayer, J. S., Zürcher, S., Lettenmaier, D. P., Beerling, D. J., Denisov, S. N., Prigent, C., Papa, F., and Kaplan, J. O.: Present state of global wetland extent and wetland methane modelling: Methodology of a model inter-comparison project (WETCHIMP), *Geosci. Model. Dev.*, 6, 617–641, <https://doi.org/10.5194/gmd-6-617-2013>, 2013.



Weber, T., Wiseman, N. A., and Kock, A.: Global ocean methane emissions dominated by shallow coastal waters, *Nat. Commun.*, 10, 1–10, <https://doi.org/10.1038/s41467-019-12541-7>, 2019.

915 Wik, M., Thornton, B. F., Bastviken, D., Uhlbäck, J., and Crill, P. M.: Biased sampling of methane release from northern lakes: A problem for extrapolation, *Geophys. Res. Lett.*, 43, 1256–1262, <https://doi.org/10.1002/2015GL066501>, 2016.

World Meteorological Organization (WMO). Greenhouse Gas Bulletin- No.17: The State of Greenhouse Gases in the Atmosphere Based on Global Observations through 2020. 2021.

920 YAK-Aerosib Measurements: <https://yak.aeris-data.fr/welcome/measurements/>, last access: 19 September 2021.

Zhang, Z., Fluet-Chouinard, E., Jensen, K., McDonald, K., Hugelius, G., Gumbrecht, T., Carroll, M., Prigent, C., Bartsch, A., and Poulter, B.: Development of the global dataset of Wetland Area and Dynamics for Methane Modeling (WAD2M), *Earth Syst. Sci. Data*, 13, 2001–2023, <https://doi.org/10.5194/essd-13-2001-2021>, 2021

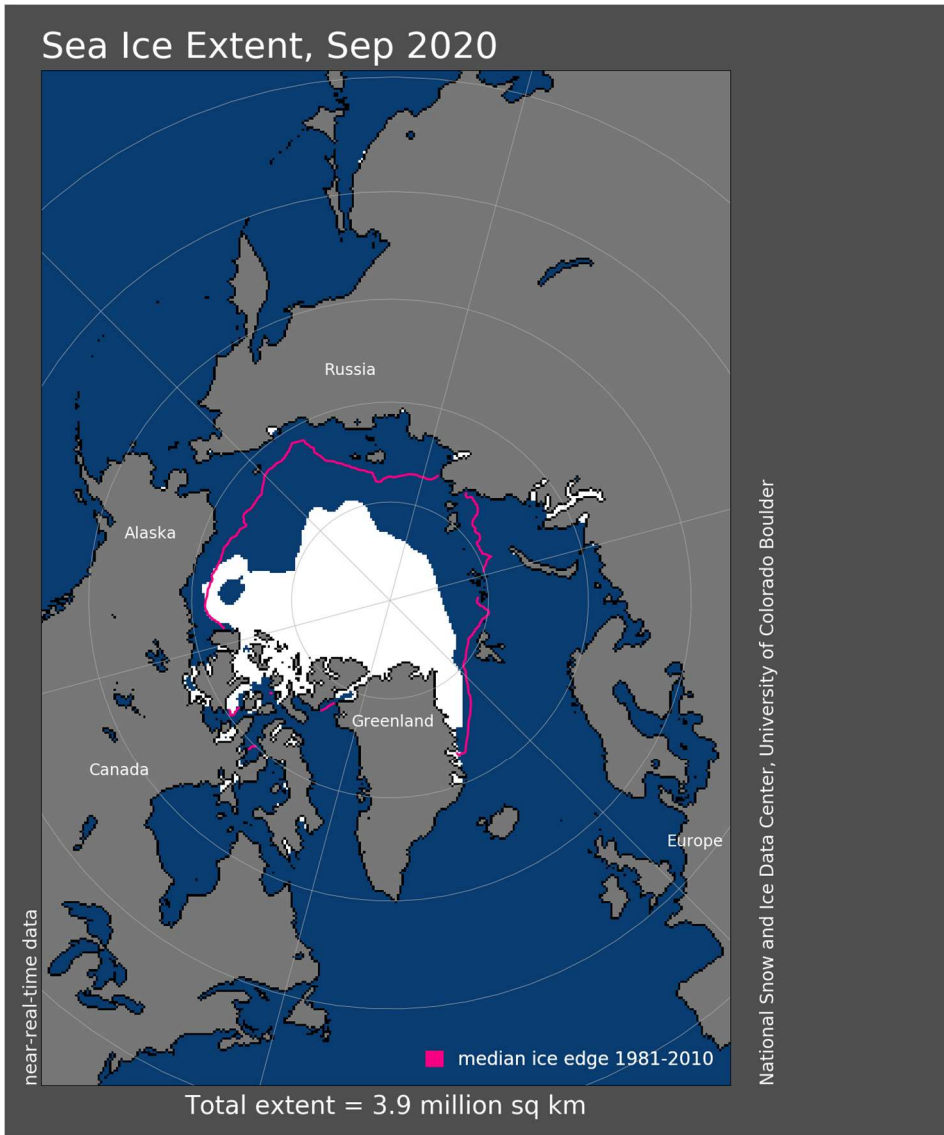


Figure A1: Sea ice extent in September 2020. As illustrated, there is no sign of ice in Bering Strait (Fetterer et al., 2017).

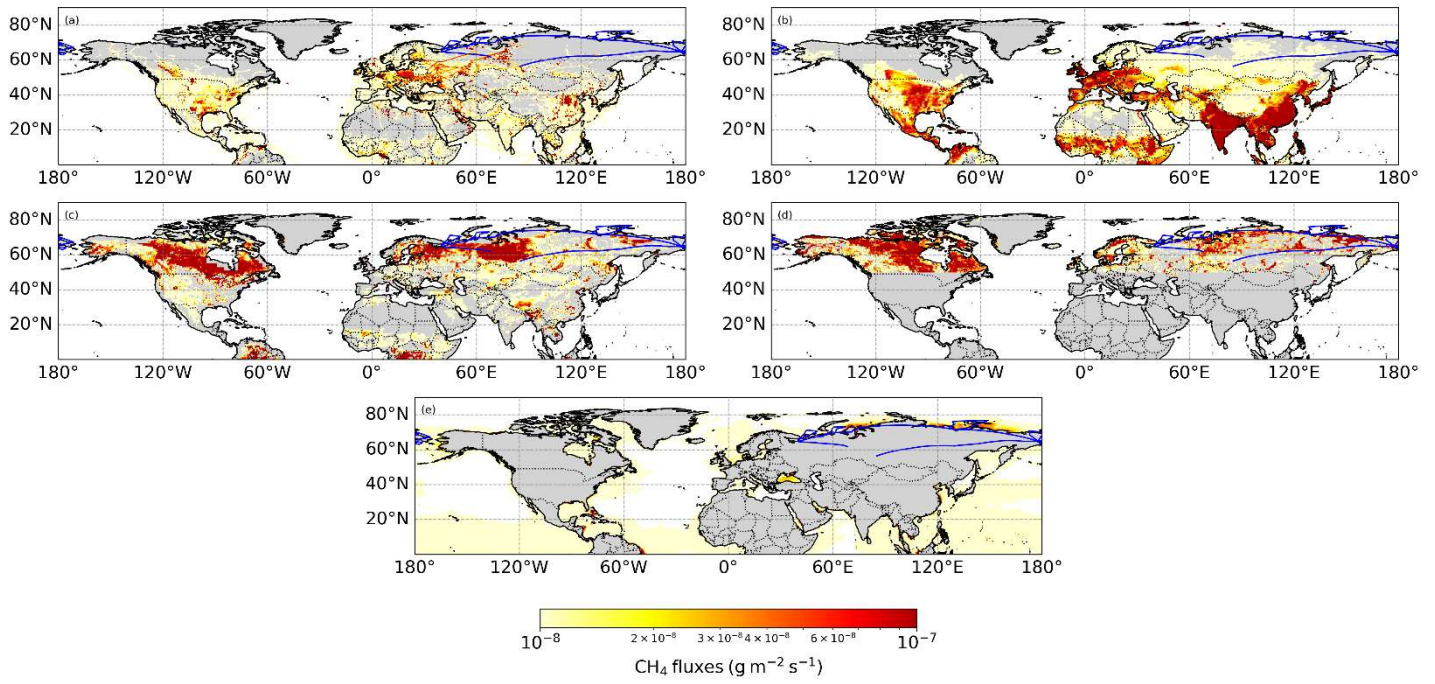
**Appendix B: Additional material on inventories**

930 **B1 EDGAR V6.0 Inventories used and sub-categories created**

**Table B1: The 21 EDGAR V6.0 inventories used for the present study regrouped in three different sub-categories.**

| Folder name      | Name                                       | Our Category          |
|------------------|--|-----------------------|
| ENE              | Power Industry                             | Fossil fuel emissions |
| REF_TRF          | Oil refineries and Transformation industry |                       |
| IND              | Combustion for manufacturing               |                       |
| CHE              | Chemical processes                         |                       |
| IRO              | Iron and steel production                  |                       |
| TNR_Aviation_CDS | Aviation climbing & descent                |                       |
| TNR_Aviation_CRS | Aviation cruise                            |                       |
| TNR_Aviation_LTO | Aviation landing & takeoff                 |                       |
| TRO              | Road transportation                        |                       |
| TNR_Other        | Railways, pipelines, off-road transport    |                       |
| TNR_Ship         | Shipping                                   |                       |
| PRO_coal         | Fuel exploitation COAL                     |                       |
| PRO_oil          | Fuel exploitation OIL                      |                       |
| PRO_gas          | Fuel exploitation GAS                      |                       |
| FFF              | Fossil fuel fires                          |                       |
| ENF              | Enteric fermentation                       | Agriculture           |
| MNM              | Manure management                          |                       |
| AGS              | Agricultural soils                         |                       |
| SWD_LDF          | Solid waste landfills                      | Waste management      |
| SWD_INC          | Solid waste incineration                   |                       |
| WWT              | Wastewater handling                        |                       |

## B2 Graphical representation of the main inventories used



935 **Figure B1:** (a) Graphical representation of CH<sub>4</sub> fluxes due to fossil fuel exploitation as reported in appendix Table A1 by EDGAR inventories. The trajectory of the campaign is represented by the blue line. (b) Same as (a) for agriculture by EDGAR. (c) same as (a) for wetlands by ORCHIDEE. (d) same as (a) for freshwaters by blake4me&GLWD. (e) same as (a) for oceans by Weber.

C1 Potential emission sensitivity (PES) under 500 m map for flight L3 at 05:01 UTC

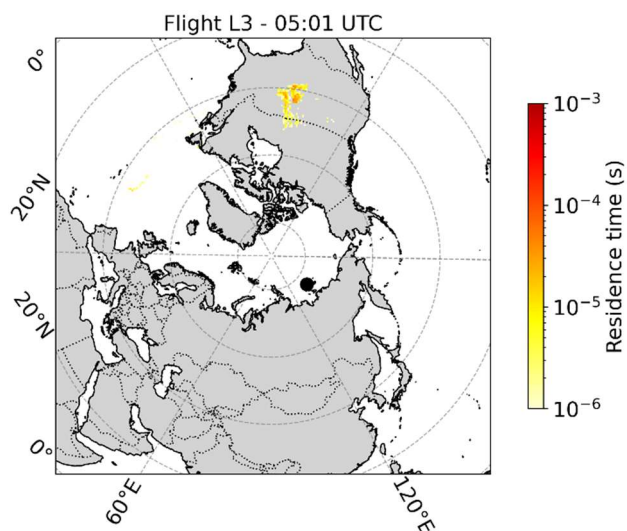


Figure C1: 10 d potential emission sensitivity (PES) with a threshold altitude of 500 m for particles released at 05:01 UTC at an altitude of 5256 m. The black dot represents the position of the receptor.

D1 Tundra around Naryan Mar



Figure D1: An aerial picture of the tundra around Naryan Mar revealing the presence of a huge number of lakes in the region. The picture was provided by Boris D. Belan.